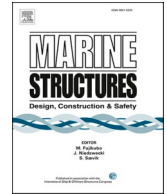




ELSEVIER

Contents lists available at [ScienceDirect](https://www.sciencedirect.com)

Marine Structures

journal homepage: <http://www.elsevier.com/locate/marstruc>

ABAQUS–OlaFlow integrated numerical model for fluid–seabed–structure interaction

Jianhong Ye ^{a,*}, Dawei Yu ^{b,a}

^a State Key Laboratory of Geomechanics and Geotechnical Engineering, Institute of Rock and Soil Mechanics, Chinese Academy of Sciences, Wuhan, Hubei, 430071, China

^b School of Engineering and Technology, China University of Geosciences (Beijing), Beijing, 100083, China

ARTICLE INFO

Keywords:

Fluid–seabed–structure interaction (FSSI)
 Integrated numerical model
 Seabed dynamics
 Residual horizontal sliding
 ABAQUS
 OlaFlow

ABSTRACT

In this study, a new one-way integrated numerical model for fluid–seabed–structure interaction is established by integrating the finite element software, ABAQUS, and the open-source fluid dynamics package, OlaFlow. In this new model, the generation and propagation of ocean waves as well as the seepage flow in a porous medium are controlled by OlaFlow; concurrently, the wave-induced dynamic responses of a porous seabed and marine structures are governed by ABAQUS. The reliability of this new model is validated by an analytical solution and a series of wave flume tests. The comparison results show that the new established model has high reliability and feasibility. Finally, this new integrated model is utilized for investigating the wave-induced dynamics of a composite breakwater and its seabed foundation as well as to evaluate the residual horizontal sliding displacement of the caisson of this composite breakwater under wave impact. Because this new integrated numerical model can fully utilize the advantages of both ABAQUS and OlaFlow, it is expected to have broad prospects for application in engineering practice.

1. Introduction

An offshore area is a valuable land resource and also the basis of marine economic development in coastal countries. In recent decades, many marine structures, such as breakwaters, pipelines, and offshore wind turbines, have been built in offshore areas. Previous studies showed that marine structures are more prone to damage than land structures [1–3]. This is because marine structures built on a porous seabed foundation are prone to failure caused by the liquefaction or shear failure of the seabed foundation under cyclic wave loading. The stability of marine structures and their seabed foundations under wave loading has generated significant attention among ocean engineers. An inappropriate design will lead to the failure and damage of marine structures in harsh ocean environments. Therefore, it is of great significance to study the problem of fluid–seabed–structure interaction (FSSI).

In the past 40 years, numerous studies were conducted on the mechanism of FSSI. Madsen [4] and Yamamoto et al. [5] first proposed analytical solutions based on Biot's consolidation theory [6] to study the wave-induced dynamics of a seabed. However, their analytical solutions could not consider the existence of marine structures built on a porous seabed. Subsequently, Hsu and Jeng [7] and Jeng and Hsu [8] proposed another analytical solution to study the dynamics of a seabed under short-crested wave loading, considering the reflection and diffraction of waves in the vicinity of the breakwater. However, a marine structure could only be simplified as a line without weight and width. A similar method was adopted by Tsai [9]. However, the effects of structural shape on wave

* Corresponding author. ,

E-mail addresses: Yejianhongcas@gmail.com, Jhye@whrsm.ac.cn (J. Ye), 3002170009@cugb.edu.cn (D. Yu).

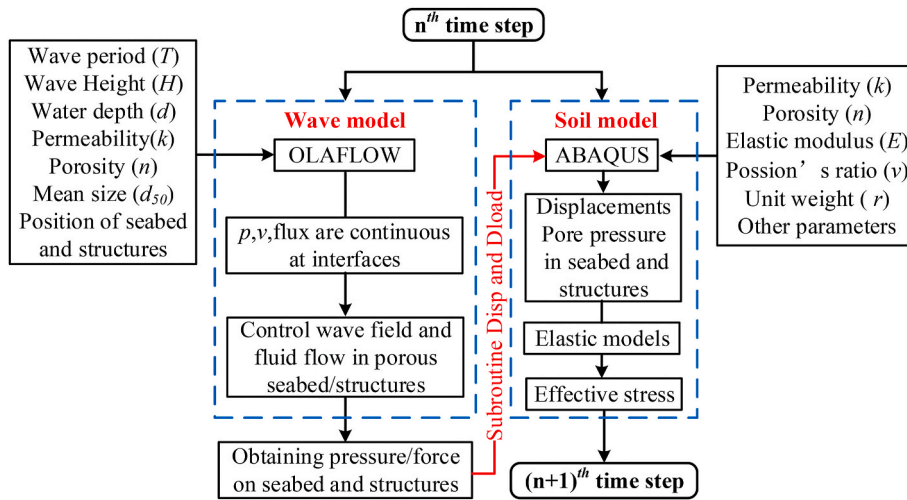


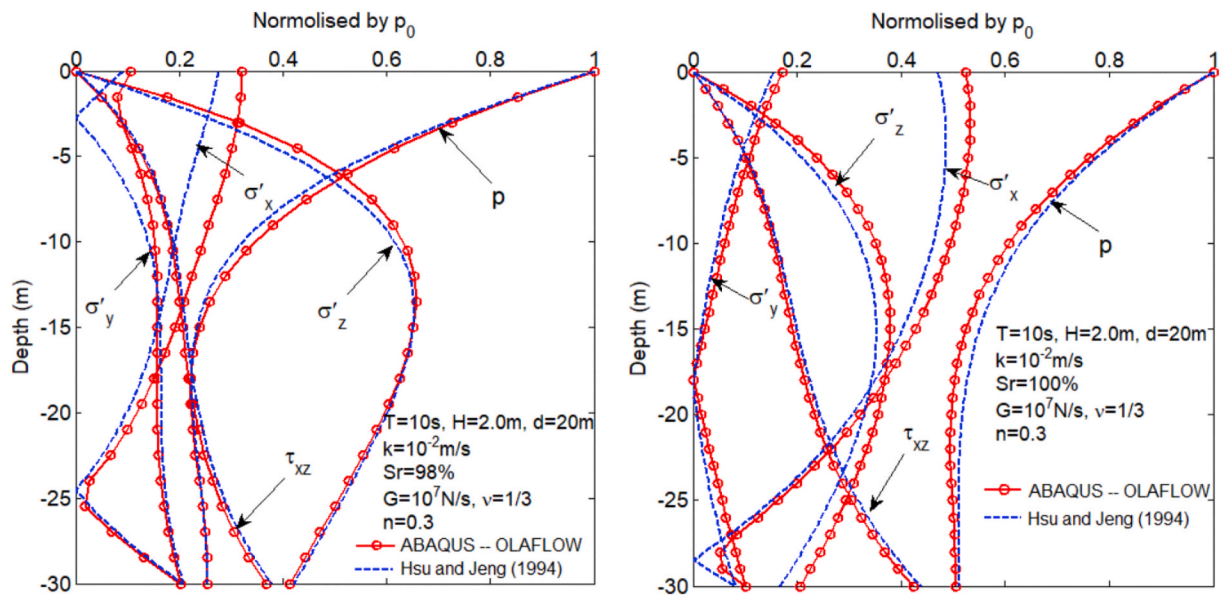
Fig. 1. Integration process of OlaFlow and soil-structure dynamics model, ABAQUS.

propagation and of structural weight on stress distribution in a seabed foundation could not be considered. In addition to analytical solutions, numerical methods were adopted to investigate wave-seabed interactions [10–12]. In these studies, linear or nonlinear Stokes waves were used to apply wave loading to the surfaces of the seabed and marine structures. Although this type of method considered the effect of structural gravity on the stress distribution in a seabed foundation, the influence of structural shape on the wave field was ignored. Because wave forces on the surfaces of marine structures could not be reliably estimated by these methods, the wave-induced dynamics of marine structures and their seabed foundation could not be reliably determined.

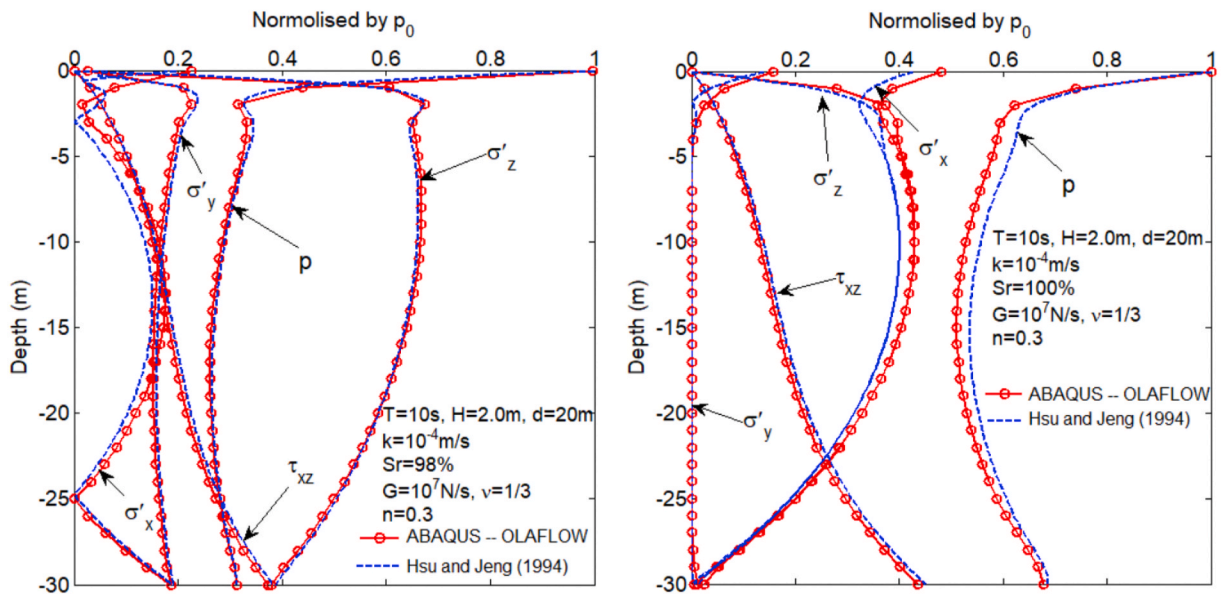
In previous studies, the Stokes wave theory was commonly used to apply a wave force on a seabed floor. Thus, the fluid exchange at the interface between seawater and pore water in a seabed foundation could not be captured. This mechanism of fluid exchange was clearly determined by Ye et al. [13]. Additionally, the wave attenuation caused by the seepage flow in a porous medium could not be considered. To overcome the above shortcomings, the drag resistance force caused by seepage flow was introduced into the Reynolds average Navier–Stokes (RANS) equation [14–16]. In particular, the volume-average Reynolds average Navier–Stokes (VARANS) equation was further proposed by Hsu et al. (2002) based on the concept of volumetric average. The VARANS equation assumes that a seabed is a rigid porous medium without a deformation potential. In this numerical modelling, by adopting the VARANS equation, the wave attenuation caused by the seepage flow in a porous seabed could be considered. However, the deformation and the effective stress in a seabed foundation and marine structures could not be determined. Subsequently, some coupled models were proposed to study the wave-induced dynamics of marine structures and their seabed foundations. For example, Mizutani and Mostafa [17] and Mostafa et al. [18] proposed integrated models of wave-seabed-structure interaction by combining a boundary element method (BEM) wave model and a finite element method soil model. The inability of previous models to determine the displacement, deformation, and stress of marine structures and their seabed foundations was overcome by these coupled models. In their models, Biot’s consolidation equation was adopted to determine the effective stresses and the displacements of marine structures and their seabed foundations. However, one of the limitations is that the effect of a complex terrain on the propagation of ocean waves cannot be naturally and effectively dealt with by the BEM model.

In recent years, many studies have also been conducted on the FSSI problem using the OpenFOAM platform [19–25] and COMSOL MultiPhysics [26–29]. However, all seabed foundations of structures were described by a poro-elastic constitutive model, and only momentary liquefaction of a seabed under wave loading was captured in the above studies. Subsequently, Zhao et al. [30]; Sui et al. [31]; Elsafti [32]; and Elsafti and Oumeraci [33] studied wave-induced residual liquefaction in the seabed foundation of marine structures by adopting empirical-based soil models or elasto-plastic soil models.

Ye et al. [34,35] and Jeng et al. [36] proposed an integrated model, FSSI-CAS-2D/3D (Fluid-Seabed-Structure Interaction, Chinese Academy of Sciences). In this model, the wave motion in the fluid domain and the seepage flow of pore water in a porous seabed were governed by the VARANS equation. Concurrently, Biot’s dynamic equation, known as ‘u–p’ approximation, was adopted to describe the displacements and effective stresses of a porous seabed and marine structures. This model implemented a one-way coupling between the wave field and the porous seabed foundation and marine structures. To the best of our knowledge, this type of one-way integrated method used in FSSI-CAS-2D/3D is yet to be broken to reach a fully coupled state. A two-way fully coupled numerical model for FSSI is still not available, in which the continuity of the displacement of the interfaces between the seabed, structures, and seawater can be implemented. In the recent decade, the FSSI-CAS-2D/3D model has been successfully used to investigate the dynamics and stability of offshore breakwaters under the regular, breaking, and tsunami wave loadings [13,37–40]. However, this model also has its shortcomings: (1) Currently, FSSI-CAS-2D/3D cannot implement parallel computing and has a relatively low computational efficiency. It is difficult to be applied in large-scale 3D cases; (2) Only a few soil constitutive models are available, and users cannot integrate their own soil constitutive models into FSSI-CAS-2D/3D; (3) There is no friendly graphical user interface (GUI), making the usage of this model complex. These shortcomings significantly limit the application of FSSI-CAS-2D/3D in engineering practice.



(a) Coarse sand



(b) Fine sand.

Fig. 2. Comparison of vertical distribution of amplitudes of wave-induced responses of seabed (T : wave period, H : wave height, d : water depth, k : permeability coefficient of soil, Sr : saturation, ν : Poisson ratio, G : elastic shear modulus, n : porosity, p_0 : amplitude of hydrodynamic loading on seabed).

Table 1
Parameters of waves and properties of sand bed in experiments conducted by Lu [41].

Wave type	Medium	H (cm)	d (m)	T (s)	G (Pa)	ν	k (m/s)	n	d_{50} (mm)	Sr
3rd Stokes	Wave	12	0.4	1.2	1.0×10^7	0.3	1.0×10^{-3}	0.3893	0.44	0.98
	Bed									
Cnoidal	Wave	12	0.3	2	1.0×10^7	0.3	1.0×10^{-3}	0.3893	0.44	0.98
	Bed									

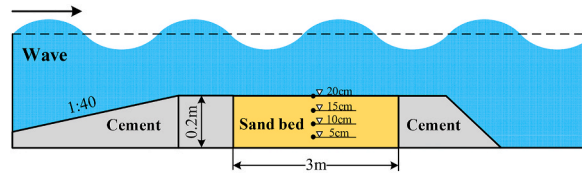


Fig. 3. Schematic of test configuration of experiments conducted by Lu [41].

To overcome these problems, for the first time, a new one-way coupling numerical model for FSSI is established in this study by integrating the finite element software, ABAQUS, and the computational fluid dynamics package, OlaFlow. Similar to FSSI-CAS 2D/3D, this new model can be used to study the dynamics and stability of marine structures and their seabed foundations under wave loading. In this new model, OlaFlow is used for the generation and propagation of waves as well as for the seepage of pore water in a porous medium; concurrently, ABAQUS is employed for computing the displacements and effective stresses of seabed foundations and marine structures. The integrated method adopted is identical to that proposed by Ye et al. [34,35]. The integrated numerical model established in this study fully utilizes the advantages of ABAQUS and OlaFlow. It is expected to have good prospects for application in engineering practice.

In this study, first, two sub-models (OlaFlow and ABAQUS) of the above-mentioned integrated model for FSSI and their coupling method are introduced. Subsequently, the reliability of the established model is verified by an analytical solution and a series of wave flume experiments. Finally, the dynamics of a composite breakwater and its seabed foundation under wave loading as well as the residual horizontal displacement of the caisson of a composite breakwater are studied using this newly established numerical model. The computational results show that the new model established in this study has good reliability. In the future, it can be employed as a reliable computational tool for evaluating the dynamics and stability of marine structures and their seabed foundations.

2. Numerical model

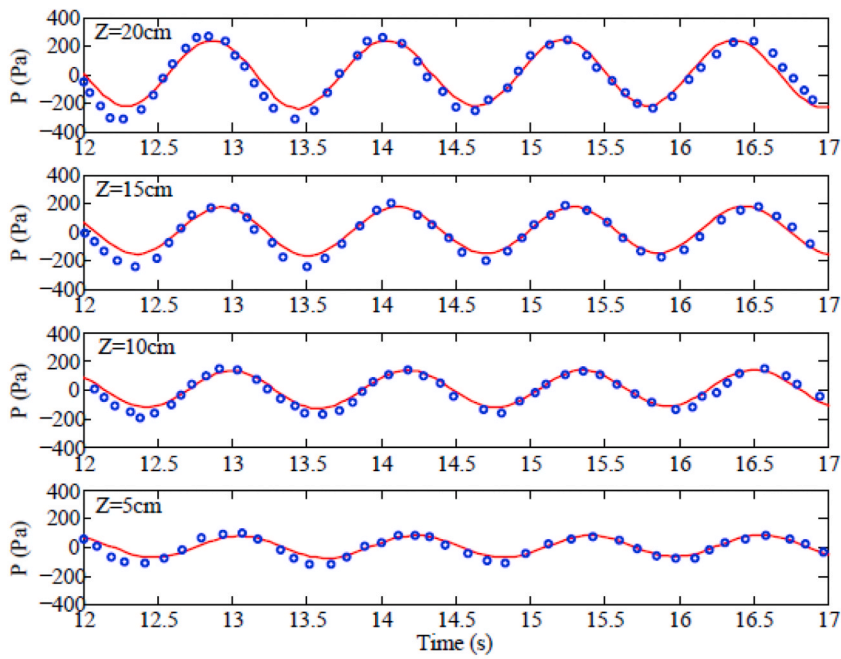
The one-way integrated numerical model for FSSI established in this study consists of two sub-models: a wave model (OlaFlow) and a soil–structure dynamics model (ABAQUS).

The wave model (OlaFlow) simulates the generation, propagation, reflection, and breaking of waves as well as of the seepage flow in a porous seabed or structures by solving the VARANS equation in the OpenFOAM framework. Importantly, a series of turbulent models, such as $k-\varepsilon$, $k-\omega$, and entropy generation models [19,20], are available in OpenFOAM. The wave-induced dynamics of a seabed foundation and a structure built on it, comprising the pore water pressure, displacement, and effective stress, are governed by ABAQUS by solving Biot's consolidation equation. ABAQUS includes a porous medium solver (referred to as 'Soils Module') for the interaction between the pore fluid and soil skeleton, which can be used to implement the involved computation.

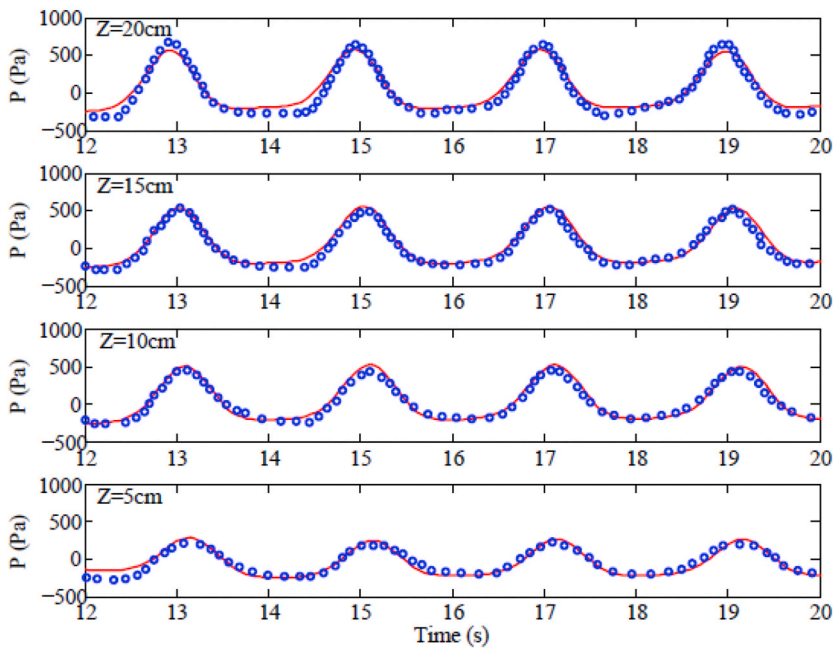
In FSSI-CAS-2D/3D, first, the one-way integrated method by Ye et al. [34,35] was adopted to apply a wave impact obtained using COBRAS (Cornell Breaking Wave and Structures) software on the surfaces of seabeds and marine structures, when investigating the interaction among waves, the seabed, and structures. In this integrated method, the pressure and flux at the interfaces between solid and fluid domains are continuous; however, a continuous displacement cannot be implemented, and the computation time steps and meshing systems of fluid and solid domains are non-matched. In the recent decade, this type of integrated method has been extensively used and recognized [24,27,29,40]. Thus far, there is no two-way fully coupled numerical model for FSSI. Although this coupling scheme cannot achieve full coupling between seabed, structures and fluid, it can basically meet the accuracy requirement under the condition of small deformation. Therefore, this integration scheme proposed by Ye et al. [34,35] is also adopted in this study.

The integration process is shown in Fig. 1. In the integration process of the wave model (OlaFlow) and the soil–structure dynamics model (ABAQUS), the impact pressure on the surface of seabed and marine structures is first determined by OlaFlow in one time step. Subsequently, the impact pressure is sent to ABAQUS via its data exchange interface subroutines, `Dload()` and `Disp()`. Finally, the wave-induced dynamics of the seabed and the marine structures, including the displacement, pore water pressure, and effective stress, can be determined using ABAQUS.

The integrated model established in this study fully utilizes a friendly GUI and parallel computation as well as a series of constitutive models available in ABAQUS. Furthermore, ABAQUS provides a secondary development interface, which enables users to incorporate their own soil constitutive models during computation. OlaFlow not only can simulate wave generation, propagation, reflection, and breaking under complex terrain conditions but also considers the attenuation of wave energy in a porous medium. Another important advantage is that both ABAQUS and OlaFlow have mature communities of users and developers, which can be utilized to answer questions about usage promptly. Furthermore, it is worth noting that ABAQUS can also be coupled with the computational fluid dynamics package, COBRAS, and analytical Stokes wave under the same framework. Thus, the application scope of this model is further extended. In summary, the integrated numerical model established in this study can fully utilize the advantages of ABAQUS and OlaFlow. It can be easily applied to large-scale engineering cases, and thus, it is expected to have good application prospects in engineering practice.



(a) Regular waves



(b) Cnoidal waves

Fig. 4. Numerically predicted results and experimental data of Lu [41] of dynamic pore pressures induced by regular and cnoidal waves (— Numerical result, ○ Experimental data).

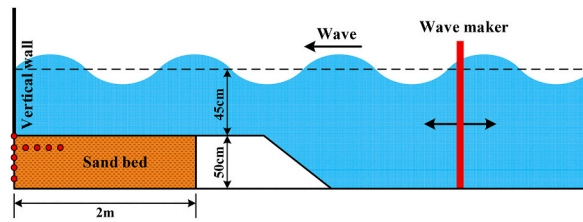


Fig. 5. Configuration of wave flume tests conducted by Tsai and Lee [9].

Table 2

Parameters of waves and properties of sand bed in experiments conducted by Tsai and Lee [9].

Wave type	Media	H (cm)	d (m)	T (s)	G (Pa)	ν	k (m/s)	n	d_{50} (mm)	Sr
2nd Stokes	Wave	5.1	0.45	1.5						
	Sand bed				2.64×10^7	0.3	1.2×10^{-4}	0.38	0.187	0.98

3. Model validation

3.1. Analytical solution

Hsu and Jeng [7] proposed an analytical solution for the dynamics of an isotropic elastic seabed with finite thickness induced by a short-crested wave. This analytical solution is used to verify the reliability of the integrated numerical model established in this study. The wave characteristics used in the numerical simulation are wave period $T = 10$ s, water depth $d = 20$ m, and wave height $H = 2.0$ m. To eliminate the influence of the lateral boundary, the seabed domain is set with a length of 200 m and thickness of 30 m.

A comparison of the vertical distribution of the amplitudes of the wave-induced responses in coarse or fine-sand seabed is presented in Fig. 2. It can be seen that the numerically predicted results are in good agreement with the analytical solution. This indicates that the newly established integrated numerical model is reliable.

3.2. Experiments by Lu [41] (regular and cnoidal waves)

Lu [41] conducted experiments to study the dynamics of a sandy bed under regular and cnoidal wave loading in a wave flume with a length of 60 m, width of 1.5 m, and height of 1.8 m. The parameters of the water waves and the properties of the sand bed are listed in Table 1. The test configuration is shown in Fig. 3. Four pore water pressure sensors were installed at distances of 5 cm between them on the central axis of the sand bed to monitor the pore water pressure during the test.

Fig. 4 (a) and (b) show the comparison of the numerically predicted results and the experimental data of the dynamic pore pressures at the four buried depths under the regular and cnoidal wave loadings, respectively. It can be seen that the numerically predicted results agree well with the experimental data of Lu [41]. This indicates that the integrated numerical model established in this study is reliable.

3.3. Experiment by Tsai and Lee [9]'s (standing wave)

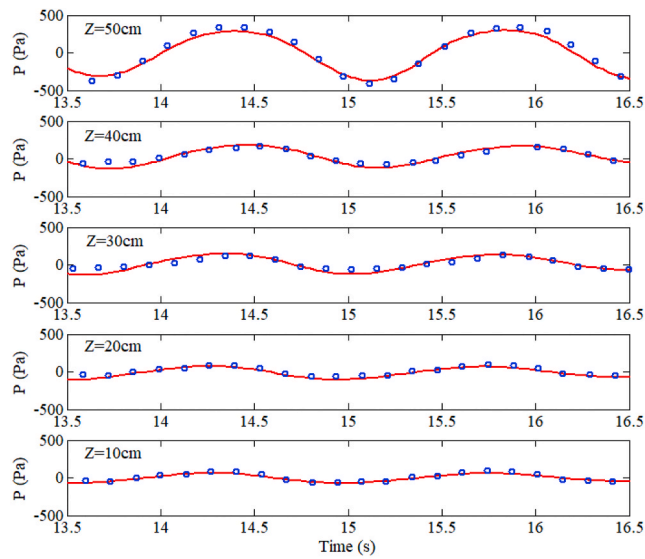
Tsai and Lee [9] conducted experiments in a wave flume 100 m long, 2 m wide, and 2 m high to verify the analytical solution proposed by them regarding the standing wave-induced seabed dynamics. The test configuration is shown in Fig. 5. In the sand bed, 11 pore water pressure sensors were installed to record the wave-induced pore pressure during testing. Five of these sensors were vertically installed with spacings of 10 cm under a vertical wall. The remaining six sensors were installed horizontally beneath the sand bed surface at distances of 10 cm. Their horizontal positions were $k_x = 0\pi, 1/10\pi, 2/10\pi, 3/10\pi, 4/10\pi,$ and $5/10\pi$, where k is the wave number. The parameters of the waves and the properties of the sand bed used in the tests are listed in Table 2.

A comparison of the numerical results predicted by the ABAQUS–OlaFlow model and the experimental data obtained by Tsai and Lee [9] is shown in Fig. 6. It can be seen that the numerical results are consistent with the experimental data.

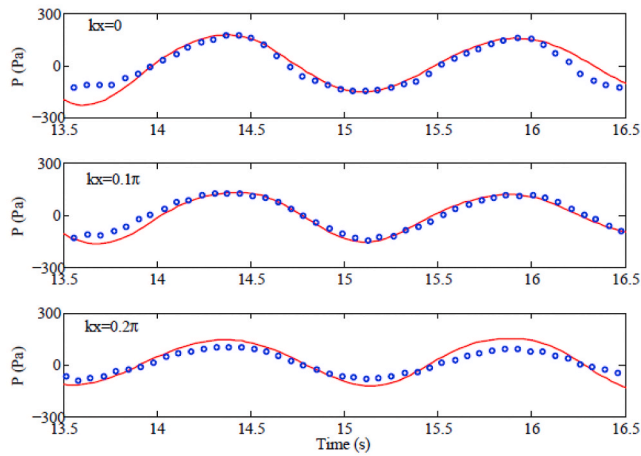
3.4. Experiment by Mizutani and Mostafa [17] (submerged breakwater)

Mizutani and Mostafa [17] conducted a set of flume tests to study the regular wave-induced dynamics of a submerged breakwater and its sand bed. The configuration of the test is shown in Fig. 7. Four wave gauges were installed in front of and behind the submerged breakwater at points a, b, c, and d, respectively, to record the wave profile. Four pore water pressure sensors were installed at points A, B, C, and D in the seabed and the breakwater to record the wave-induced pore water pressure. The parameters of the waves and the properties of the sand bed used by Mizutani and Mostafa [17] are listed in Table 3.

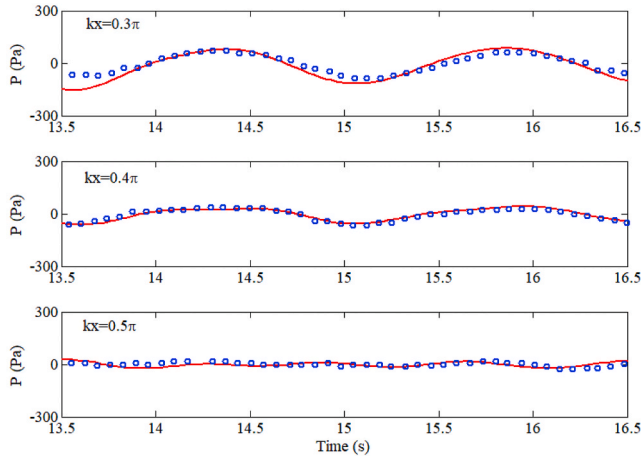
Figs. 8 and 9 present the comparison of the wave profiles and wave-induced pore water pressures obtained from the numerical



(a) Pore pressure along vertical wall



(b) Pore pressure along horizontal direction ($0\pi-0.2\pi$)



(c) Pore pressure along horizontal direction ($0.3\pi-0.5\pi$)

(caption on next page)

Fig. 6. Comparison of wave-induced pore pressures obtained numerically and experimentally by Tsai and Lee [9] (— Numerical result, ○ Experimental data).

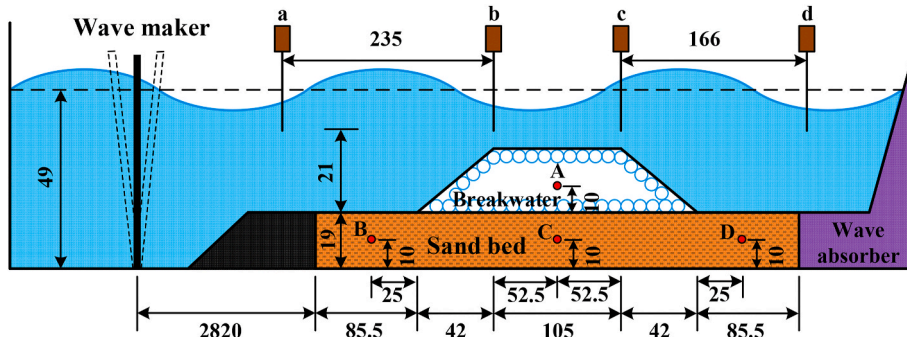


Fig. 7. Configuration of wave flume tests conducted by Mizutani and Mostafa [17] (Unit: cm).

Table 3

Parameters of waves and properties of sand bed used in tests conducted by Mizutani and Mostafa [17].

Wave type	Medium	H (cm)	d (m)	T (s)	G (Pa)	ν	k (m/s)	n	d_{50} (mm)	Sr
2nd Stokes	Wave	3	0.3	1.4						
	Sand bed				5.0×10^8	0.33	2.2×10^{-3}	0.3	1	0.99
	Breakwater				1.0×10^9	0.24	1.8×10^{-1}	0.33	30	0.99

predictions and the experiments conducted by Mizutani and Mostafa [17]. It can be seen that the predicted wave profiles at points a, b, c, and d are consistent with the measured profiles, and the predicted pore pressures at points A, B, C, and D agree well with the measured ones.

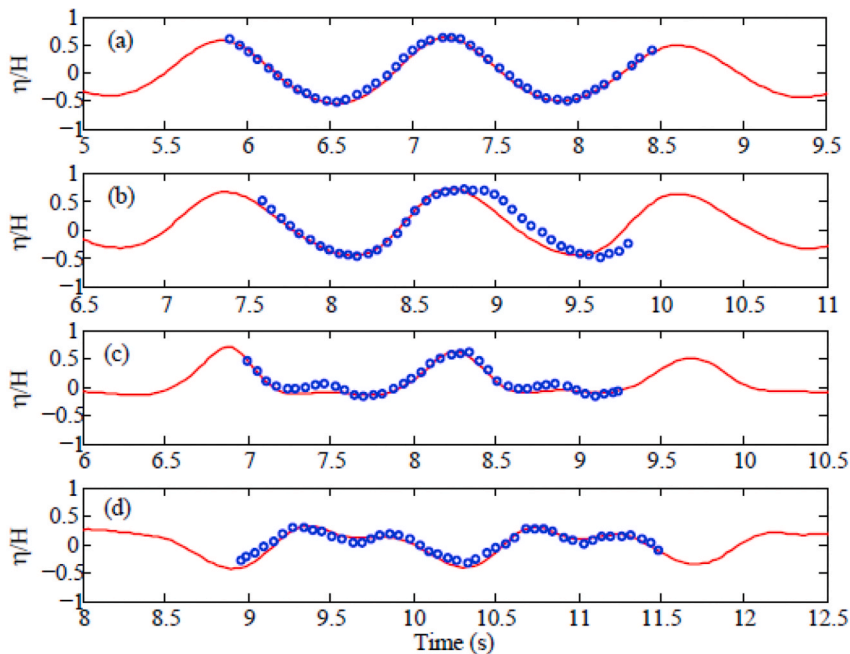


Fig. 8. Wave profiles obtained from numerical predictions and experiments conducted by Mizutani and Mostafa [17] (— Numerical result, ○ Experimental data).

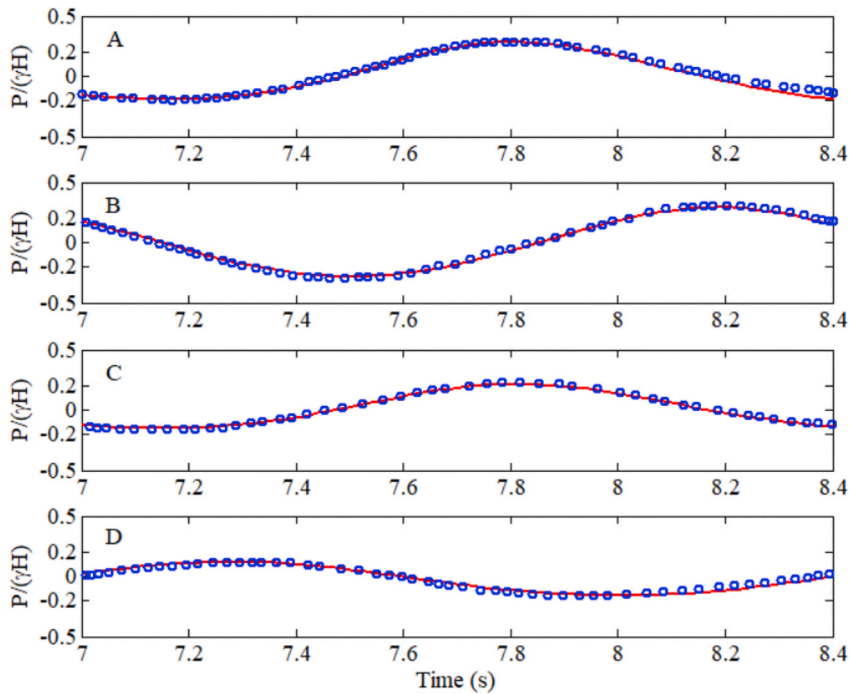


Fig. 9. Comparison of wave-induced pore pressures obtained from numerical predictions and experiments conducted by Mizutani and Mostafa [17] (— Numerical result, ○ Experimental data).

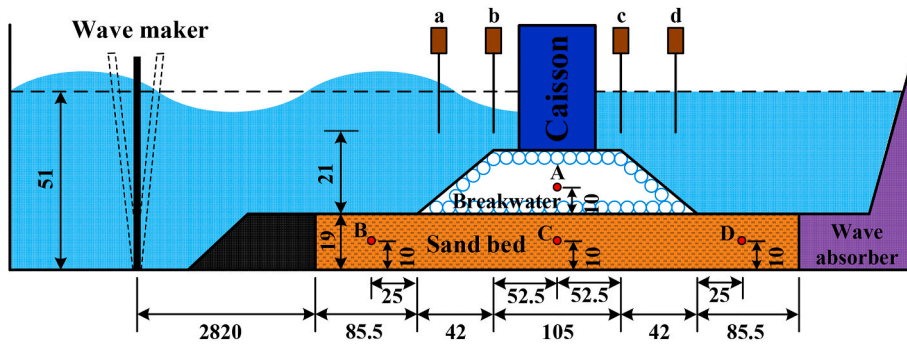


Fig. 10. Configuration of wave flume tests conducted by Mostafa et al. [18] (Unit: cm).

Table 4

Parameters of waves and properties of sand bed used in experiments by Mostafa et al. [18].

Wave type	Medium	H (cm)	d (m)	T (s)	G (Pa)	ν	k (m/s)	n	d_{50} (mm)	Sr
2nd Stokes	Wave	5	0.32	2.2						
	Sand bed				5.0×10^8	0.33	2.2×10^{-3}	0.3	0.8	0.98
	Rubble mound				1.0×10^9	0.24	1.6×10^{-1}	0.33	27	0.99

3.5. Experiment by Mostafa et al. [18] (Composite breakwater)

Based on the wave flume tests for a submerged breakwater conducted by Mizutani and Mostafa [17]; Mostafa et al. [18] performed a series of wave flume tests for a composite breakwater in the same wave flume to study the wave-induced dynamics of the composite breakwater and its sand bed foundation. The configuration of the test is shown in Fig. 10. The parameters of the waves and the properties of the sand bed used by Mostafa et al. [18] are listed in Table 4.

A comparison of the wave profiles and wave-induced pore pressures obtained from the numerical prediction and the experiments conducted by Mostafa et al. [18] is illustrated in Figs. 11 and 12. Because the caisson is an impermeable medium, which typically

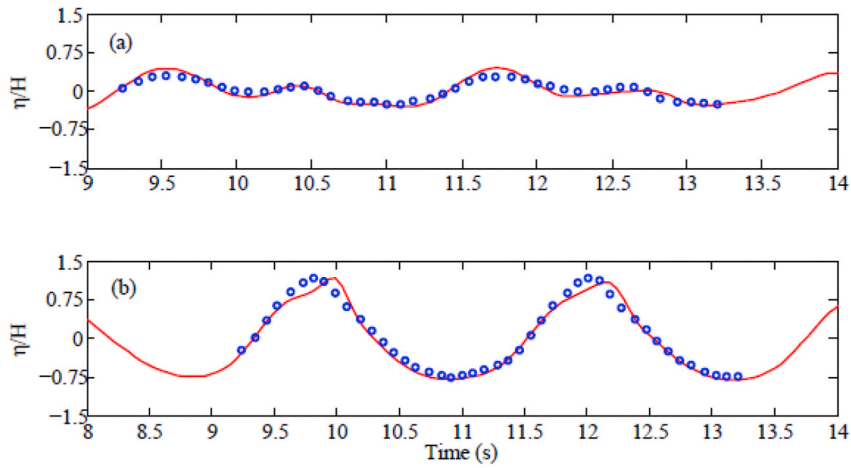


Fig. 11. Wave profiles obtained from numerical prediction and experiments by Mostafa et al. [18] (— Numerical result, ○ Experimental data).

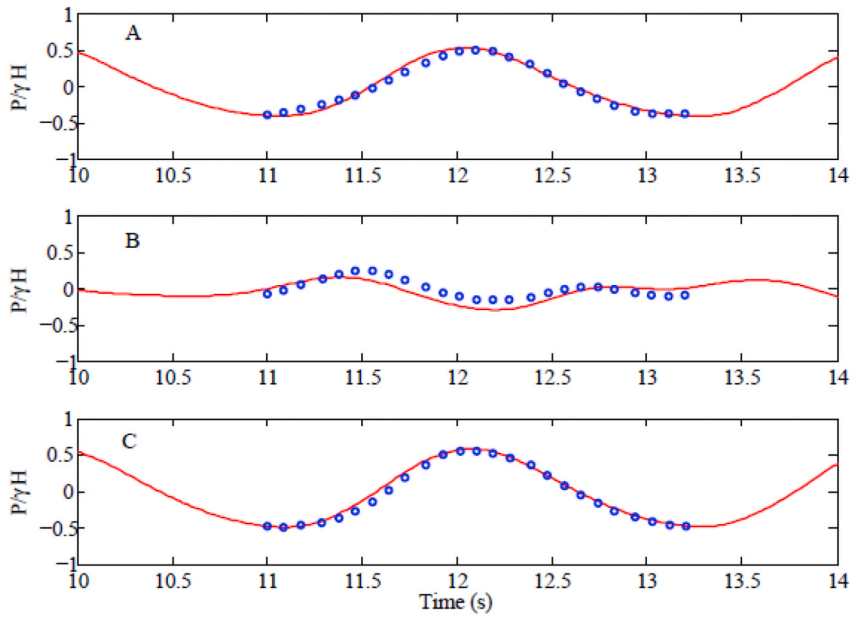


Fig. 12. Comparison of the wave-induced pore pressure obtained from numerical prediction and experiments conducted by Mostafa et al. [18] (— Numerical result, ○ Experimental data).

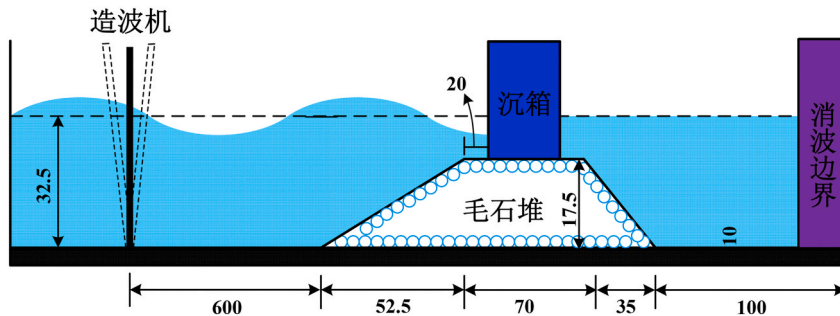


Fig. 13. Configuration of wave flume tests conducted by Wang et al. [42] (Unit: cm).

Table 5
Parameters of waves and properties of rubble mound used by Wang et al. [42].

Rubble mound property	Medium	H (cm)	d (cm)	T (s)	G (Pa)	ν	n	d_{50} (mm)	S_r
Impermeable	5th wave	16.7	32.5	1.3					
Permeable	5th wave	16.7	32.5	1.3					
	Rubble mound				1.0×10^9	0.24	0.45	8	0.99

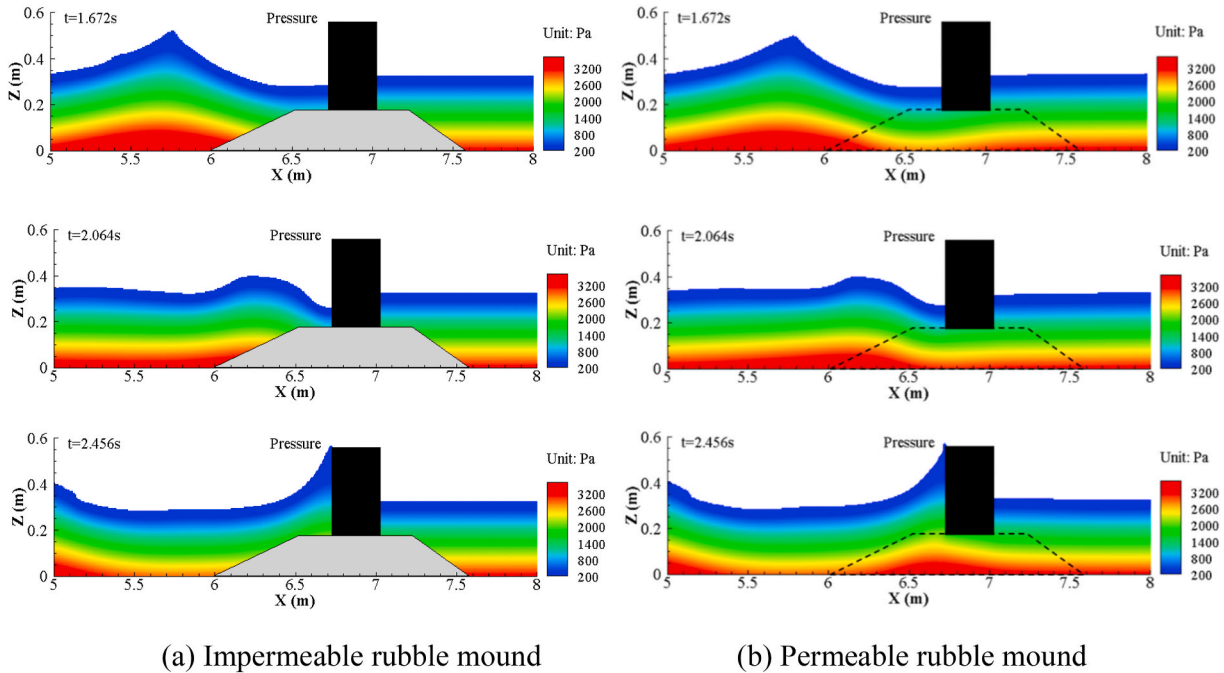


Fig. 14. Pressure distributions around caisson at three typical moments.

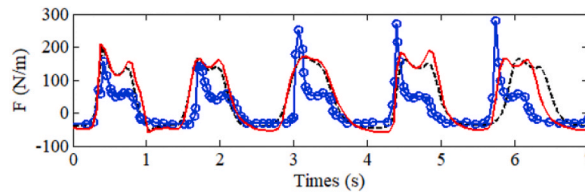


Fig. 15. Comparison of horizontal impact forces on caisson obtained from numerical prediction and tests (--- Experimental data, —●— Numerical result with permeable rubble mound, — Numerical result with impermeable rubble mound).

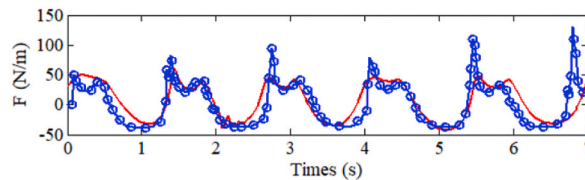


Fig. 16. Comparison of numerical and test results of buoyancy at the bottom of caisson (— Numerical result, —●— Experimental data with permeable rubble mound).

blocks the propagation of waves, the fluctuation of the water surface on the right side of the composite breakwater is very small. Consequently, it is difficult for the wave gauges to record the wave profiles on the right side of the composite breakwater. Therefore, only the wave profiles at points *a* and *b* are compared with the test data in Fig. 11. It is seen that the numerically predicted wave profiles

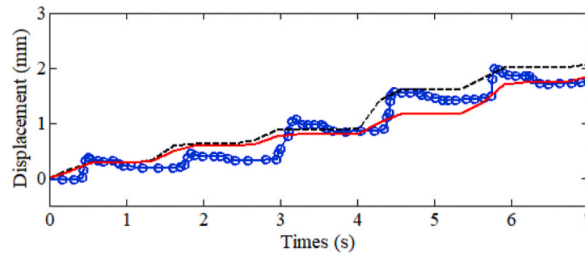


Fig. 17. Comparison of numerical and test results of horizontal residual displacement of caisson (--- Experimental data, — Numerical result with permeable rubble mound, — Numerical result with impermeable rubble mound).

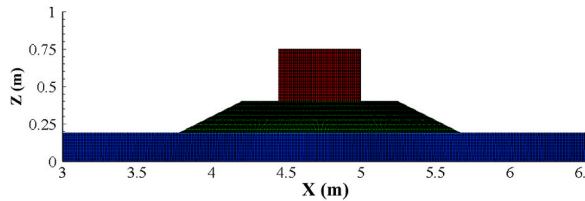


Fig. 18. Finite element mesh generated in computational domain.

and pore water pressures are in good agreement with the measured data.

3.6. Experiment by Wang et al. [42] (Caisson sliding)

Wang et al. [42] conducted wave flume tests for a composite breakwater in a wave flume of length 30 m, width 1 m, and height 1 m to study the horizontal residual displacement of a caisson under a cyclic wave impact, as illustrated in Fig. 13. The integrated numerical model established in this study is used to reproduce the test process as well as to predict the wave impact pressure and the residual horizontal displacement of the caisson. Subsequently, the numerical results and the experimental data are compared to verify the reliability of the integrated numerical model. The density of the caisson was 1440 kg/m^3 . The friction coefficients at the interface between the caisson and the rubble mound were 0.501 and 0.54 when the interface is and is not immersed in water, respectively. A series of impermeable blocks were pieced together to form a rubble mound foundation in the test. Consequently, the water filling the gaps between these blocks in the rubble mound foundation of the composite breakwater could provide buoyancy to the overlying impermeable caisson. To identify the effect of the buoyancy, sliding processes of the caisson were studied under impermeable and permeable rubble mound foundations. Because the basic parameters of the rubble mound were not provided by Wang et al. [42]; the parameters of the rubble mound foundation were estimated based on the typical range of the physical properties of rubble mounds, as listed in Table 5.

Fig. 14 (a) shows the water pressure distribution around the caisson at three typical times when the rubble mound is treated as an impermeable block. It is observed that at $t = 1.672 \text{ s}$, a wave crest is moving towards the breakwater. At $t = 2.064 \text{ s}$, the wave crest approaches the caisson. It can be seen from the wave profile that the wave has a clear reflection and superposition after it arrives at the rubble mound. At $t = 2.456 \text{ s}$, the wave crest climbs along the lateral side of the caisson. From the wave profile at $t = 2.456 \text{ s}$, it can be seen that the wave exceeds the highest point of the caisson. A slight wave overtopping occurs thereafter. Fig. 14 (b) shows the water pressure distribution around the caisson at the same three typical times when the rubble mound is treated as a permeable medium. Based on the comparative analysis, it is found that the pressure distributions around the caisson are basically the same at the three typical moments, regardless of the rubble mound being treated as an impermeable or permeable medium in the computations. The only difference is that pore pressure fluctuation occurs in the rubble mound foundation if it is permeable.

Fig. 15 illustrates the measured and numerical results of the horizontal impact forces on the caisson under the conditions of permeable and impermeable rubble mounds. It can be seen that although the impact characteristics obtained from the numerical prediction are less clear than those from the experiments, they are approximately consistent. Simultaneously, the impact force on the caisson under the condition of a permeable rubble mound is slightly less than that under the condition of an impermeable rubble mound. This is because when the rubble mound is treated as a permeable medium, the wave energy can be partly attenuated owing to the seepage process of the pore water in the rubble mound. From the time history of the impact force on the breakwater caisson illustrated in Fig. 15, it can be observed that there is a phase difference at the later stage between the two numerical results under the conditions of permeable and impermeable rubble mounds. Overall, the effect of the property of the rubble mound (impermeable or permeable) on the wave-induced impact force on the caisson is insignificant.

A comparison of the experimental and numerically predicted results of the buoyancy on the caisson bottom under the condition of a permeable rubble mound is shown in Fig. 16. It is found that the numerically predicted values basically agree with the experimental data. This buoyancy on the caisson bottom has a significant effect on the dynamics and horizontal residual displacement of the caisson.

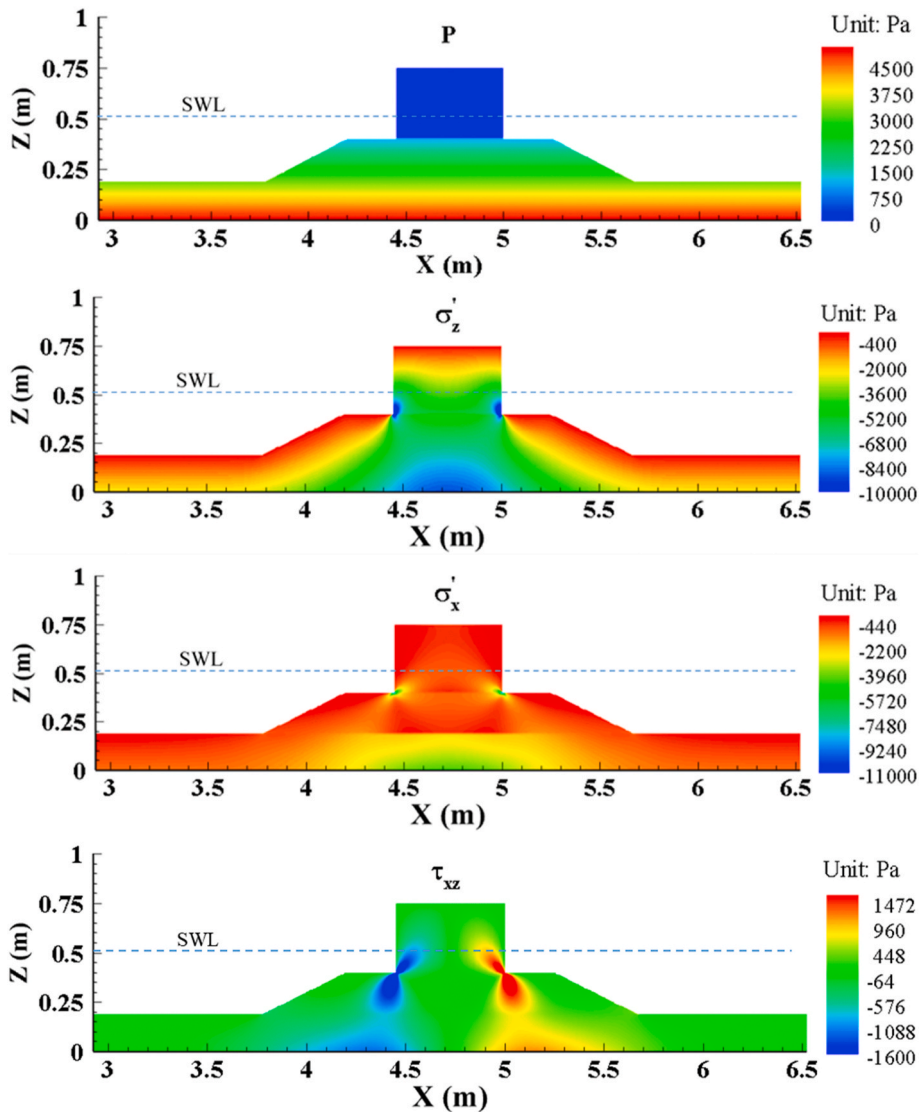


Fig. 19. Distributions of pore pressures and effective stresses in initial equilibrium state.

If this buoyancy is considered, the horizontal residual displacement will be underestimated, as shown in Fig. 17.

Fig. 17 illustrates the comparison of the horizontal residual displacements of the caisson obtained from the tests and the numerical prediction (with permeable and impermeable rubble mound) under a cyclic wave impact. It can be seen that the numerically predicted results of the horizontal residual displacement agree with the experimental results. This indicates that the integrated numerical model established in this study has good reliability.

However, an interesting phenomenon can be observed in Figs. 15 and 17. The impact force on the caisson under the condition of a permeable rubble mound is slightly less than that in the case of an impermeable rubble mound, as illustrated in Fig. 15. However, the horizontal residual displacement of the caisson under the former condition is more remarkable than that under the latter condition, as shown in Fig. 17. This is because the upward dynamic buoyancy on the bottom of the caisson is considered when the rubble mound is permeable. Consequently, the friction force against the horizontal sliding between the caisson and the rubble mound is smaller than when the buoyancy is not considered. Therefore, although the impact force on the caisson is slightly less, the horizontal residual displacement of the caisson is still greater if the rubble mound is treated as a permeable medium than that when considered as an impermeable one.

4. Model application 1: wave-induced dynamics of offshore structure and its seabed foundation

In this section, taking the configuration of the wave flume test conducted by Mostafa et al. [18] as an example, the integrated numerical model for FSSI established in this study is used to study the dynamics (dynamic pore pressure and effective stress) of the

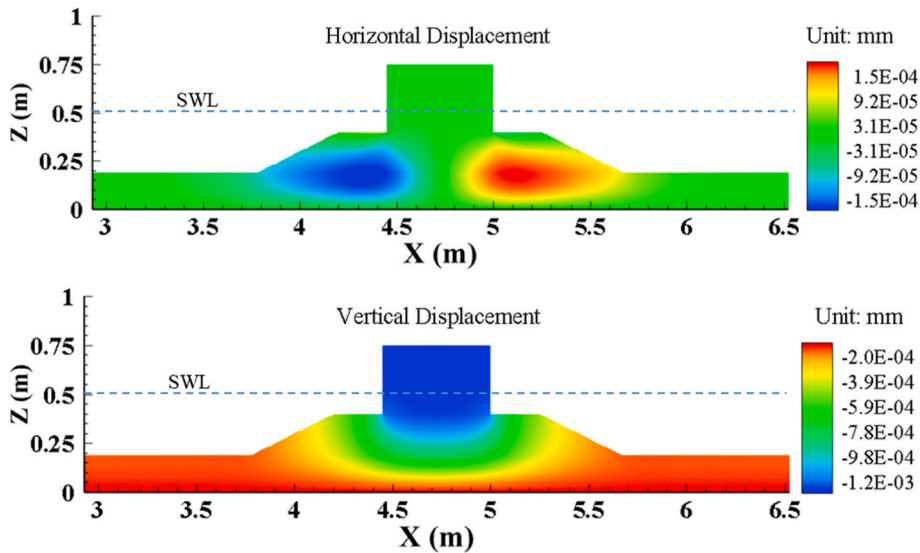


Fig. 20. Distributions of displacements of breakwater and its sand foundation in initial state.

small-scale composite breakwater and its sand foundation under wave loading. The configuration is previously described in Section 3.5 and illustrated in Fig. 10. The computational domain and the generated mesh are shown in Fig. 18. A total of 15742 CPE4P elements are used for the sand foundation and the rubble mound and 3465 CPE4 elements for the rigid caisson to discretize the computational domain. The mesh size is approximately 1 cm. The boundary conditions in ABAQUS are set as follows: (1) Both horizontal and vertical displacements of the bottom of the sand foundation are fixed. (2) The horizontal displacements of the two lateral sides of the sand foundation are fixed. (3) The bottom of the sand bed is set as an impermeable boundary. (4) Sum of the dynamic wave pressure and the hydrostatic pressure determined by OlaFlow is applied on the surface of the sand foundation and the composite breakwater at each time step. A total of 553400 finite volume elements are used to discretize the fluid domain. The maximum mesh size in the zone far away from the breakwater is 0.2 cm. It is only 0.1 cm in the zone around the breakwater. The wave parameters as well as the properties of the sand foundation and the composite breakwater used in the computation are listed in Table 4. The caisson density is set as 1400 kg/m³.

4.1. Initial state

Before a water wave attacks the composite breakwater, the composite breakwater and its sand foundation must be in an equilibrium state. This initial equilibrium state should be considered as the initial condition in the subsequent dynamic analysis. The correctness of the determined initial equilibrium state directly affects the reliability of the subsequent analysis results. Therefore, it is necessary to first determine the initial equilibrium state.

The initial pore pressures and the effective stresses in the composite breakwater and its sand foundation under gravitational weight are illustrated in Fig. 19. The pore water pressure is distributed in layers in the rubble mound and the sand foundation. Because the caisson is treated as an impermeable rigid body, its pore pressure is zero. Because of the compression caused by the breakwater, σ'_x and σ'_z in the sand foundation under it are clearly greater than those in the other zones. σ'_x and σ'_z are also distributed in layers in the zone away from the breakwater. It is also observed that two symmetrical concentration zones are formed for τ'_{xz} inside the rubble mound and the sand foundation.

Fig. 20 illustrates the distributions of the horizontal and vertical displacements of the breakwater and its sand foundation in the initial state. It is found that the breakwater is slightly subsided, because of which the foundation soil under it moves towards the lateral sides.

4.2. Dynamics of breakwater and sand foundation

The wave-induced pore pressures and effective stresses in the breakwater and its sand foundation at a typical moment ($t = 17.65$ s) are presented in Fig. 21 under the conditions of $H = 0.3$ m, $d = 0.5$ m, and $T = 2.0$ s.

At $t = 17.65$ s, a wave crest is attacking the caisson. In Fig. 21, it can be seen that the wave-induced dynamic pore pressures in the rubble mound and the sand bed are significant at this moment. The distribution of dynamic σ'_x indicates that the breakwater tends to slide to the right side because of the rightward impact when the wave crest arrives at the caisson. Thus, the left side of the rubble mound is stretched, forming a tensile dynamic stress zone at $t = 17.65$ s. Concurrently, the right side of the rubble mound is compressed, forming a compressive dynamic stress zone. It is also observed that a concentration zone of the shear stress is formed around

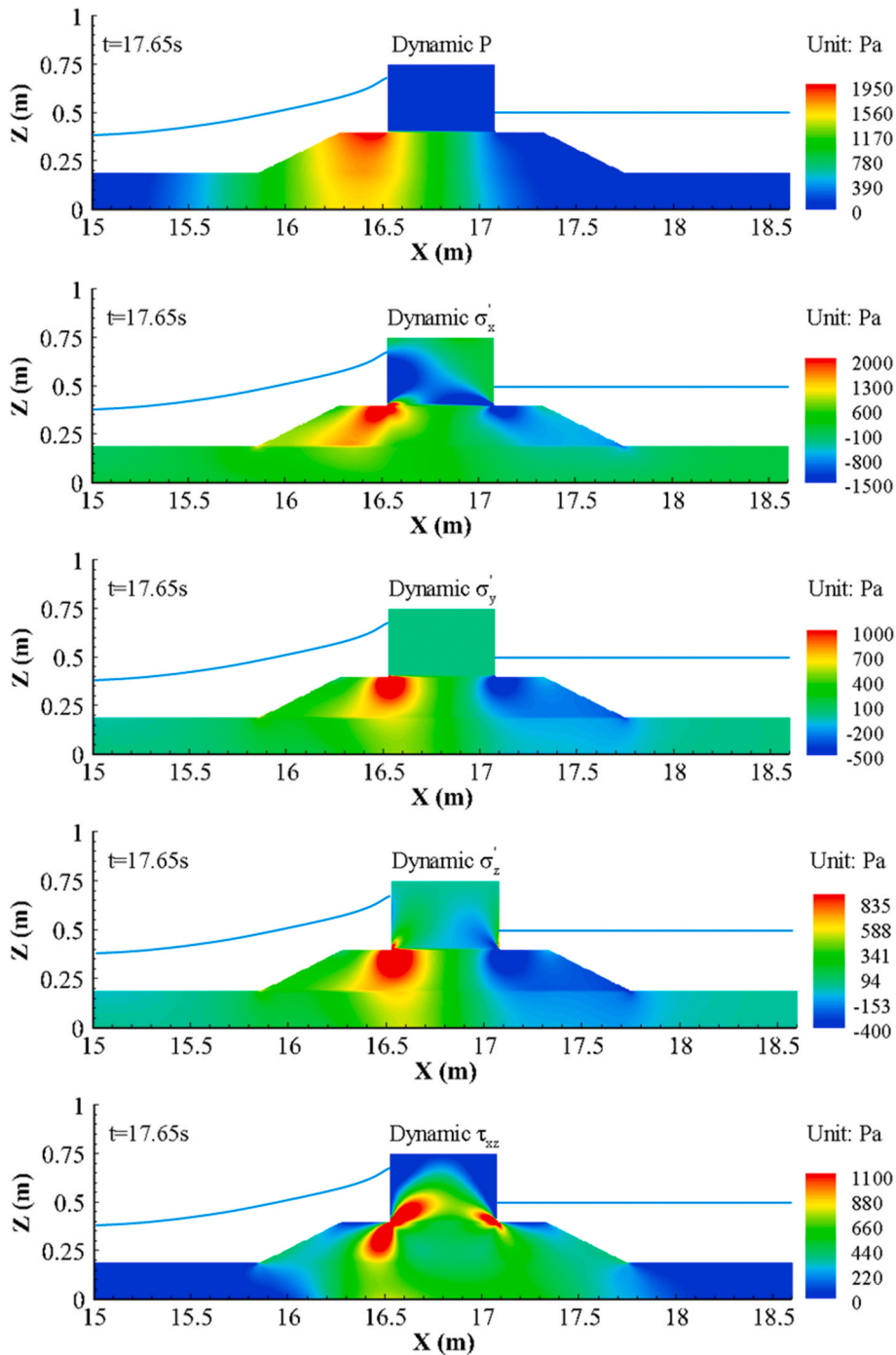


Fig. 21. Distributions of wave-induced dynamic pore pressure and effective stresses in breakwater and its sand foundation at $t = 17.65\text{ s}$.

the left lower part of the caisson and in the rubble mound. When the caisson and the rubble mound are set as separated objects and the contacting algorithm is applied to the interface between them in ABAQUS, the caisson slides to the right side once the wave impact exceeds the frictional resistance. The analysis of this behaviour of the caisson is discussed in the next section.

The time histories of the wave-induced displacements of the caisson are shown in Fig. 22. The caisson vibrates under the wave loading. Even though the magnitudes of the displacements are small, they can still be captured by the integrated numerical model established in this study.

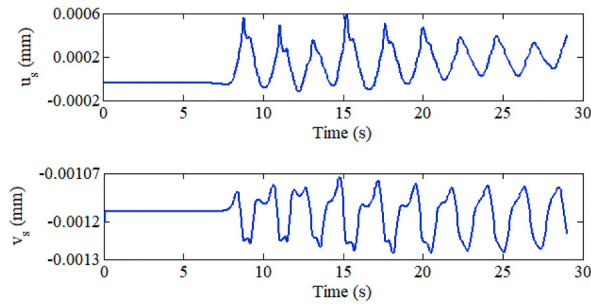


Fig. 22. Time histories of displacements occurring at the upper left corner of caisson (u_s : horizontal displacement, v_s : vertical displacement).

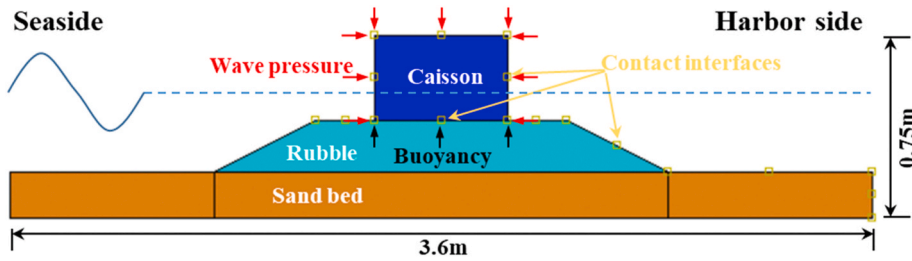


Fig. 23. Schematic of contact setting and boundary condition for wave impact.

Table 6

Wave parameters, friction coefficients at interface, and final residual sliding.

H (m)	d (m)	T (s)	Wave order	Friction coefficient μ	Final residual sliding (mm)
0.2	0.5	2	5th	0.10	220
				0.15	420
				0.20	72
				0.25	19
				0.30	6.4

Table 7

Wave parameters, friction coefficients at interface, and final residual sliding.

H (m)	d (m)	T (s)	Wave order	Friction coefficient μ	Final residual sliding (mm)
0.3	0.5	2	5th	0.1	635
				0.2	460
				0.3	80
				0.4	2.3
				0.5	0.006

Table 8

Wave parameters, friction coefficients at interface, and final residual sliding.

H (m)	d (m)	T (s)	Wave order	Friction coefficient μ	Final residual sliding (mm)
0.4	0.6	2	5th	0.1	1100
				0.2	630
				0.3	420
				0.4	340
				0.5	0.59

5. Model application 2: residual horizontal sliding of caisson

In the last decade, numerous studies have been conducted on wave–seabed–breakwater interactions [12,23,26,40]. However, the contact interaction between a caisson and the underlying rubble mound is typically dealt by establishing a weak thin layer at their

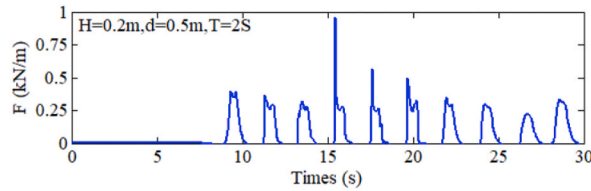


Fig. 24. Time history of wave impact applied on caisson when $H = 0.2$ m, $d = 0.5$ m, and $T = 2$ s.

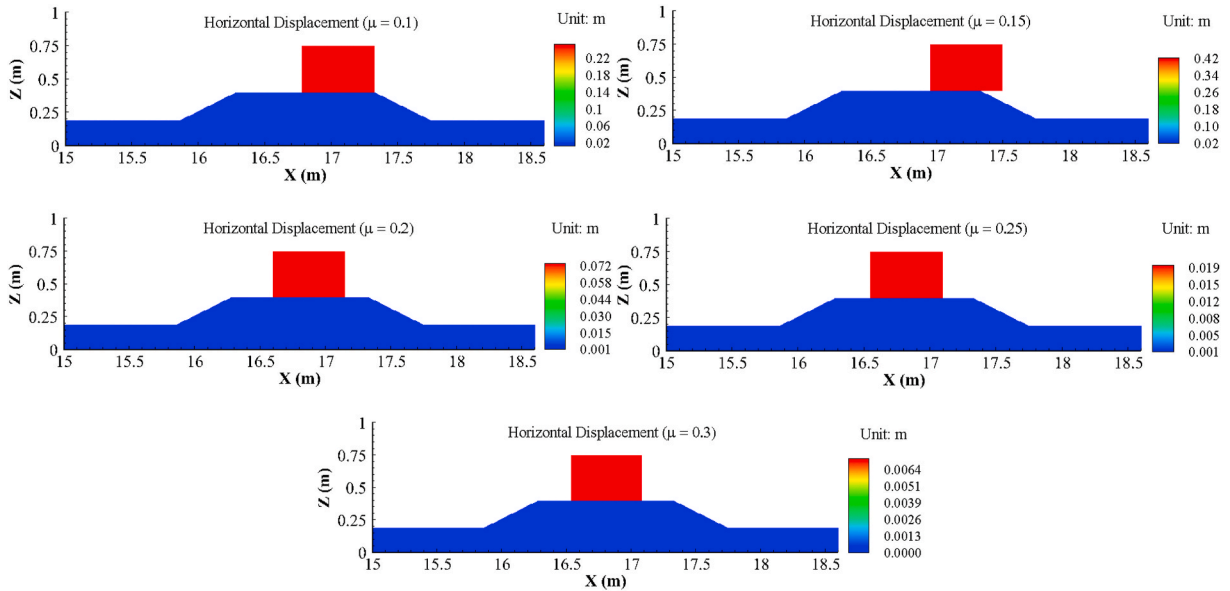


Fig. 25. Residual horizontal sliding of caisson with different friction coefficients at the end of computation when $H = 0.2$ m, $d = 0.5$ m, and $T = 2$ s.

contacting surface [43,44]. Consequently, the caisson and the underlying rubble mound are connected together through some common nodes on their contact surface in the numerical modelling. Thus, the movement of a caisson can only be caused by the deformation of a thin contacting layer, and it cannot produce a larger sliding than its underlying rubble mound. The residual horizontal sliding displacement of a caisson relative to its underlying rubble mound is generally difficult to determine using previous models. This is a shortcoming of most previously published studies. The tilting or collapse of a caisson due to its excessive sliding relative to its underlying rubble mound driven by a wave impact is also a critical failure mode in engineering practice.

This section presents the adoption of the new integrated model established in this study to determine the residual sliding displacement of a caisson under the impact of water waves using the powerful function available in ABAQUS to solve the contact problems. The configuration illustrated in Fig. 10 is continued to be chosen as the typical case. A schematic of the contact setting between the caisson and its underlying rubble mound as well as the boundary condition for the wave impact are shown in Fig. 23. In the numerical analysis, the outer surface of the caisson is set to potentially contact the surface of the rubble mound and the right-side of the upper surface of the sand bed foundation when the caisson is moving under the wave impact. In particular, the upward buoyancy on the bottom of the caisson is applied to prevent the underestimation of the residual sliding displacement of the caisson, as illustrated in Fig. 17.

Because the module ‘Soils’ in ABAQUS for the interaction between the pore fluid and soil skeleton does not contain a function to deal with the contact and friction between objects, the integrated numerical model established in this study must be simplified to estimate the wave-induced residual sliding displacement of the caisson. The composite breakwater and its sand bed foundation are treated as two independent impermeable elastic bodies, and the pore water in the rubble mound and the sand bed cannot be considered in the computation. The sliding of the caisson relative to the rubble mound and its sand bed foundation is simulated by the contact algorithm available in the modulus, ‘Dynamic-implicit’ of ABAQUS. The normal contact is set as a hard contact, and a friction coefficient (μ) is set for the tangential contact. The wave impact and the buoyancy determined by the wave model (OlaFlow) are applied to the surface of the caisson in the computation. It should be noted that the wave is generated according to the 5th Stokes wave theory in OlaFlow.

Three types of wave conditions are applied based on different wave heights and water depths. They are (1) $H = 0.2$ m, $d = 0.5$ m, $T = 2$ s; (2) $H = 0.3$ m, $d = 0.5$ m, $T = 2$ s; (3) $H = 0.4$ m, $d = 0.6$ m, $T = 2$ s. Under each wave condition, five different friction coefficients are set for the interface between the rubble mound and the caisson. Thus, a total of 15 cases are implemented to record the residual

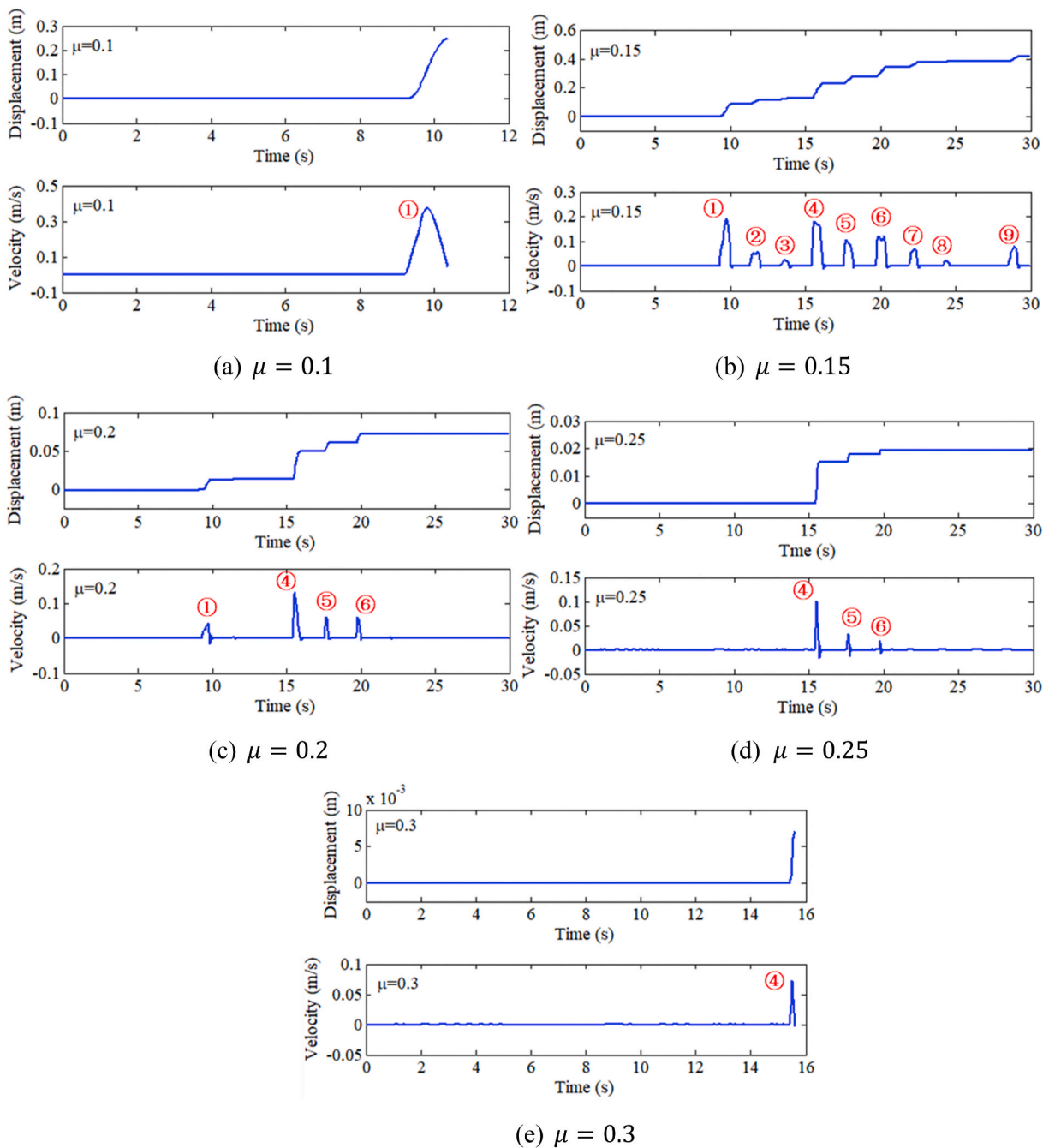


Fig. 26. Time histories of horizontal sliding and corresponding velocity of caisson.

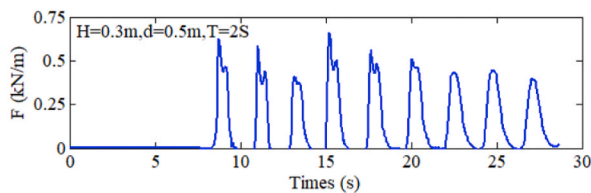


Fig. 27. Time history of impact force on caisson when $H = 0.3\text{ m}$, $d = 0.5\text{ m}$, and $T = 2\text{ s}$.

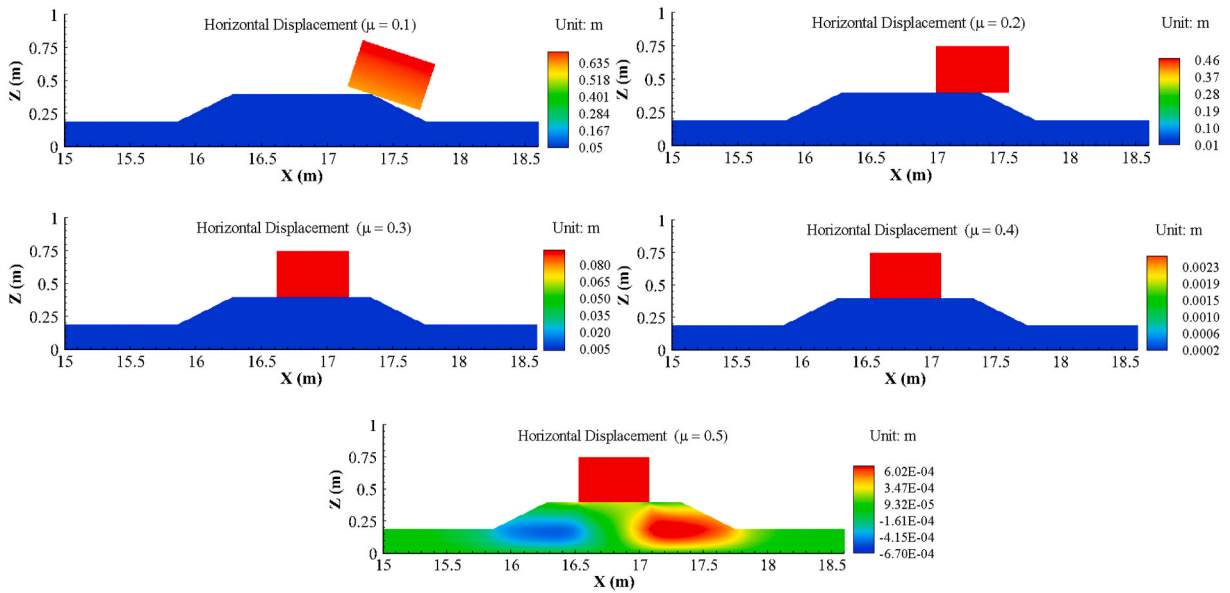


Fig. 28. Residual horizontal displacements of caisson with different friction coefficients when $H = 0.3$ m, $d = 0.5$ m, and $T = 2$ s.

horizontal sliding of the caisson. The wave parameters, friction coefficient settings, and computational residual horizontal sliding of the caisson are listed in Tables 6–8.

5.1. $H = 0.2$ m, $d = 0.5$ m, and $T = 2$ s

Fig. 24 shows the time history of the wave impact force applied on the lateral side of the caisson when $H = 0.2$ m, $d = 0.5$ m, and $T = 2$ s. It can be seen in Fig. 25 that the peak wave impact force on the caisson is mostly less than 500 N; however, occasionally it also increases up to 900 N at $t = 15.2$ s.

The residual horizontal sliding of the caisson, when the friction coefficient, μ , varies from 0.1 to 0.3 and when $H = 0.2$ m, $d = 0.5$ m, and $T = 2$ s at the end of the computation is illustrated in Fig. 25. It can be seen that the residual horizontal displacement of the caisson gradually decreases as μ increases from 0.1 to 0.3. However, interestingly, the residual sliding of the caisson is 0.22 m when $\mu = 0.1$, which is less than that (0.42 m) when $\mu = 0.15$, as listed in Table 6. This may be because the wave impact force applied on the caisson is much greater than the frictional resistance force induced by the gravity weight of the caisson when $\mu = 0.1$ at the early stage of the wave impact. The caisson instantly tends to rotate in a short time. The sharp bottom right corner of the caisson intrudes into the rubble mound during the rotation. Thus, the mesh of the rubble mound is severely distorted, which further causes convergence problem in the computation. If the numerical convergence can be ensured, the final residual sliding when $\mu = 0.1$ will definitely be greater than that when $\mu = 0.15$. This explanation is clearly supported by the time history of the sliding process of the caisson illustrated in Fig. 26 (a) and (b).

The time histories of the horizontal sliding and the corresponding velocity of the caisson for different μ values when $H = 0.2$ m, $d = 0.5$ m, and $T = 2$ s are shown in Fig. 26. It can be seen that the caisson presents a considerable displacement when the first wave crest reaches it, at $\mu = 0.1$. However, the computation is stopped at $t = 10.5$ s owing to the numerical convergence problem. Under the condition of $\mu = 0.15$, based on Fig. 26 (b), the caisson slides rightward in each wave period. After a total of nine wave impacts, the residual horizontal displacement of the caisson reaches approximately 0.42 m. However, the caisson does not collapse, as exhibited in Fig. 25. From Fig. 26 (c) and (d), it can be seen that the caisson can only slide when the peak wave impact force is relatively large because of which the frictional resistance force between the caisson and the rubble mound becomes greater when $\mu = 0.2$ or 0.25. When $\mu = 0.3$, the caisson only slides 6.4 mm rightward under the fourth wave impact. However, the computation is also stopped owing to the convergence problem.

5.2. $H = 0.3$ m, $d = 0.5$ m, and $T = 2$ s

The time history of the wave impact force on the caisson when $H = 0.3$ m, $d = 0.5$ m, and $T = 2$ s is shown in Fig. 27. It can be seen that the peak wave impact force is 680 N. Compared to the peak wave impact force illustrated in Fig. 24, the peak wave impact force when $H = 0.3$ m is generally greater than that when $H = 0.2$ m. However, interestingly, the maximum peak wave impact force when $H = 0.3$ m is less than that when $H = 0.2$ m. However, this phenomenon only occurs at one time at approximately $t = 16$ s.

The residual horizontal sliding of the caisson, when the friction coefficient, μ , varies from 0.1 to 0.5 and when $H = 0.3$ m, $d = 0.5$ m, and $T = 2$ s at the end of the computation are illustrated in Fig. 28. It can be seen that the residual sliding of the caisson decreases from

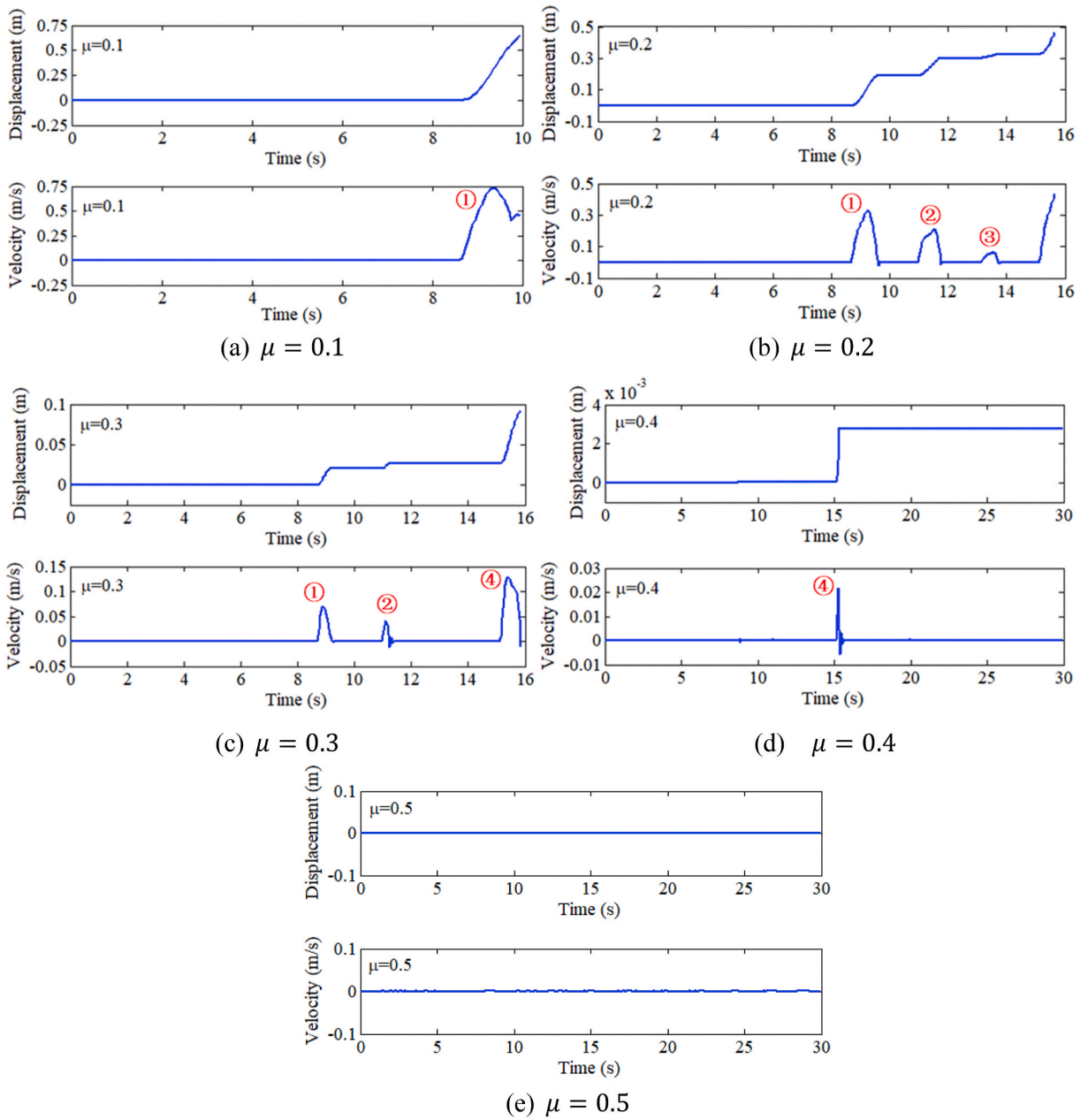


Fig. 29. Time histories of horizontal sliding and corresponding velocity of caisson.

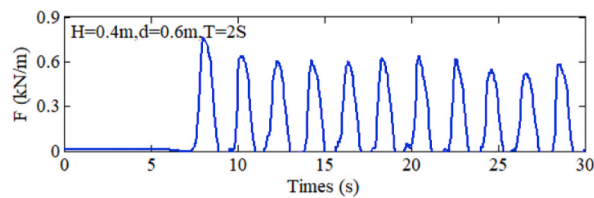


Fig. 30. Time history of impact force on caisson when $H = 0.4$ m, $d = 0.6$ m, and $T = 2$ s.

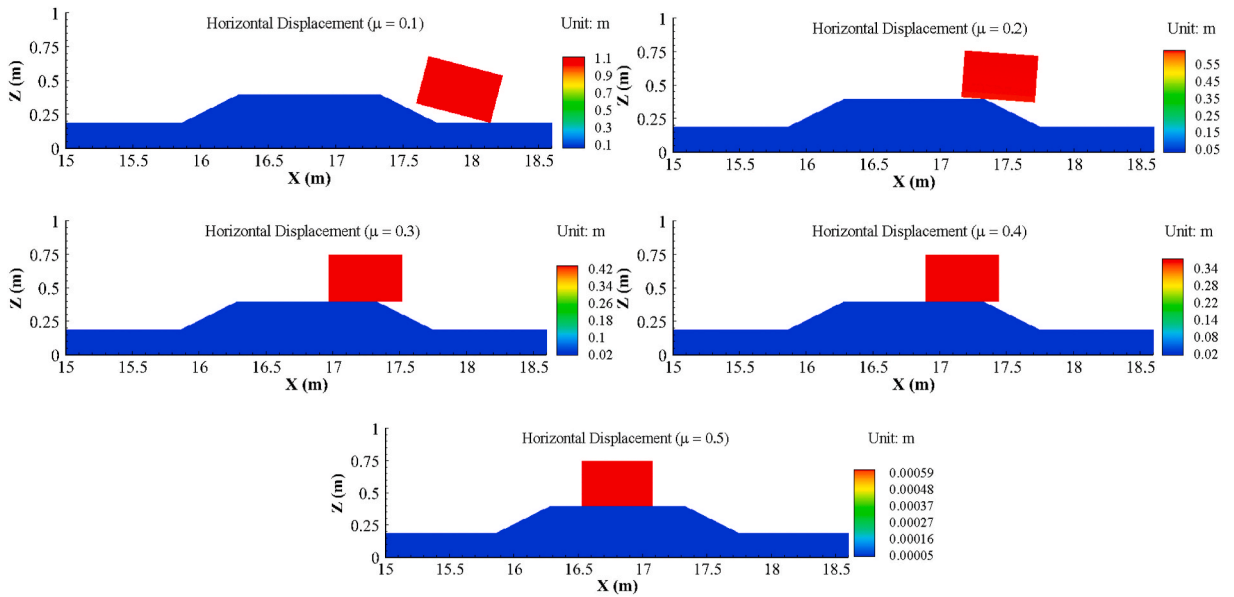


Fig. 31. Residual horizontal displacements of caisson with different friction coefficients when $H = 0.4$ m, $d = 0.6$ m, and $T = 2$ s.

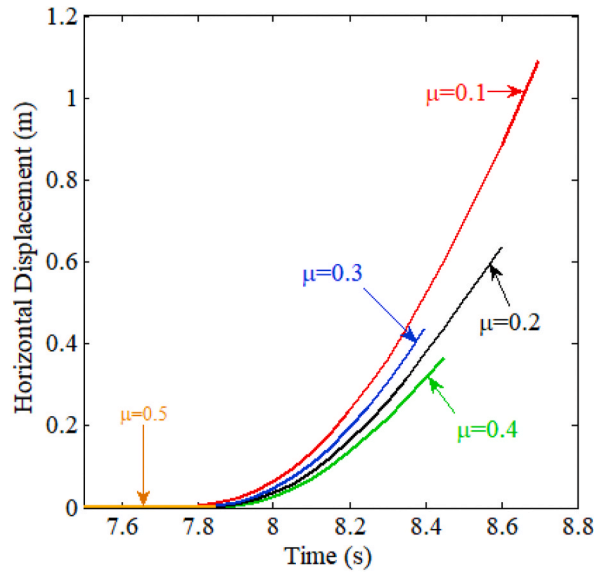


Fig. 32. Time histories of residual horizontal sliding of caisson with different μ ($H = 0.4$ m, $d = 0.6$ m, $T = 2$ s).

635 mm to 0.6 mm as μ increases from 0.1 to 0.5, which can also be seen in Table 7. It is also interesting to note that the caisson collapses at the end of the computation when $\mu = 0.1$ owing to the low resistance to the sliding at the interface.

The time histories of the horizontal sliding and the corresponding velocity of the caisson for different μ values when $H = 0.3$ m, $d = 0.5$ m, and $T = 2$ s are shown in Fig. 29. It can be seen that the caisson also has a considerable displacement when the first wave crest reaches it when $\mu = 0.1$. However, the computation is stopped at $t = 10$ s owing to the numerical convergence problem. The reason for this convergence problem is already discussed in Section 5.1. Accordingly, the caisson can only slide when the wave impact force is greater than the frictional resistance force at the interface between the caisson and the rubble mound when $\mu = 0.2$ – 0.4 . It is also interesting that the caisson basically has no residual sliding when $\mu = 0.5$ under the impact of the water wave as seen in Fig. 29 (e).

5.3. $H = 0.4$ m, $d = 0.6$ m, and $T = 2$ s

The time history of the wave impact force on the caisson when $H = 0.4$ m, $d = 0.6$ m, and $T = 2$ s is shown in Fig. 30. It can be seen

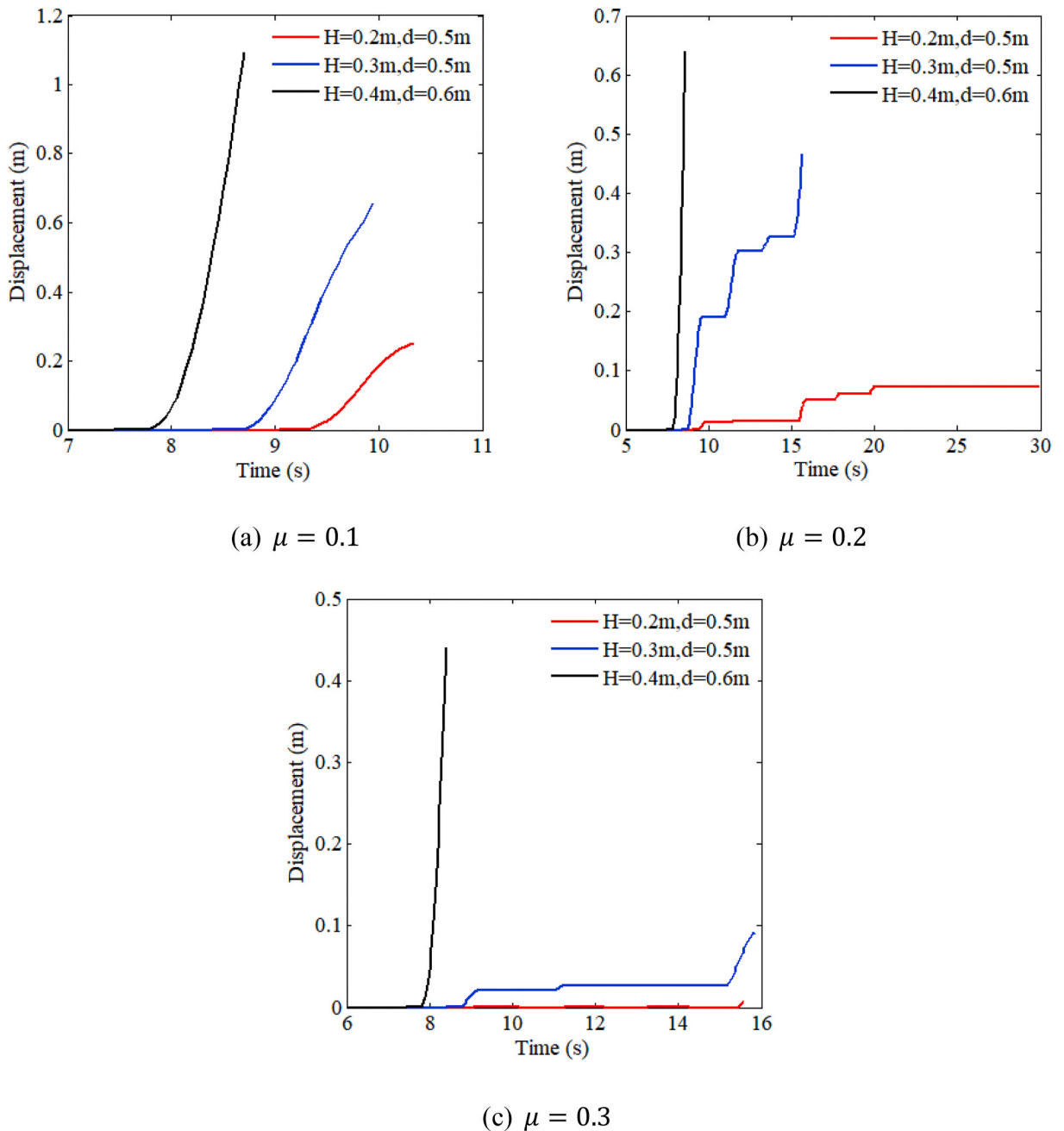


Fig. 33. Time histories of residual horizontal sliding of caisson with different friction coefficients and different wave heights.

that the peak wave impact force is generally greater than 600 N and can maximally reach up to 800 N. Compared to the wave impact forces illustrated in Figs. 24 and 27, the peak wave impact force is generally greater.

The residual horizontal sliding of the caisson, when the friction coefficient, μ , varies from 0.1 to 0.5 and when $H = 0.4$ m, $d = 0.6$ m, and $T = 2$ s at the end of the computation are illustrated in Fig. 31. Combined with Table 8, it can be seen that the residual sliding of the caisson is much more considerable than that illustrated in Sections 5.1 and 5.2. The maximal residual sliding of the caisson is approximately 1100 mm when $\mu = 0.1$, as can be seen from Table 8. Overall, the final residual sliding of the caisson is also negative to the friction coefficient, μ , at the interface. In Fig. 31, it is also observed that the caisson collapses when $\mu = 0.1$, and it is near to collapse when $\mu = 0.2$. Under the condition of $\mu \geq 0.3$, only horizontal sliding occurs without collapse.

The time histories of the horizontal sliding of the caisson for different μ values when $H = 0.4$ m, $d = 0.6$ m, and $T = 2$ s are shown in Fig. 32. It can be seen that the caisson slides considerably when the first wave crest reaches the caisson when $\mu \leq 0.4$. The computation is stopped because of the non-convergence problem in the first wave period. The residual sliding of the caisson is only 0.59 mm when μ

= 0.5 owing to the strong frictional resistance at the interface.

Finally, the time histories of the horizontal sliding of the caisson for different wave heights and different friction coefficients are presented in Fig. 33. It is clearly seen that the higher the wave height, the greater the residual displacement of the caisson when the friction coefficient is the same.

The integrated model established in this study has issues when dealing with the pore water in rubble mounds and sand bed foundations, and there is a non-convergence problem in some cases. However, it should be noted that it can still effectively and approximatively deal with the problem of estimation of the residual horizontal sliding of a caisson under a wave impact. This strongly supports the application of the integrated model established in this study in engineering practice in the future.

6. Conclusion

A new integrated numerical model for FSSI is established by integrating OlaFlow (wave model) and ABAQUS (soil dynamics model) in this study. Specifically, the wave motion and the pore water seepage in a porous seabed are governed by OlaFlow, and the wave-induced dynamics of marine structures and their seabed foundations are controlled by ABAQUS. A series of laboratory wave flume tests and an analytical solution proposed by Hus and Jeng [7] are used to verify the established integrated numerical model. The verification indicates that the established integrated numerical model for the FSSI problem is reliable. The experimental configuration of the wave flume test conducted by Mostafa et al. [18] is taken as a typical case. The wave-induced dynamics of a composite breakwater and its seabed foundation, and the wave-induced residual horizontal sliding of the caisson of the composite breakwater are comprehensively studied by adopting the integrated numerical model established in this study. Based on the study presented here, the following conclusions are drawn:

- 1) Compared with previous models, the newly established integrated numerical model for FSSI in this study has the following advantages: (1) both ABAQUS and OlaFlow can be run in parallel with high efficiency; (2) OlaFlow can reliably simulate the complex process of wave breaking, reflection, and superposition after a wave encounters structures; (3) Secondary development at a higher level can be conducted, and the programming interface for the development of soil constitutive models is available in ABAQUS. (4) ABAQUS and OlaFlow are being commonly used worldwide, and there are some very mature online communities available for the users and developers. This will enable excellent promotion for of this new FSSI model.
- 2) When the integrated numerical model established in this study is applied to analyse the wave-induced dynamics of structures and their seabed foundations, the dynamic variation in the effective stresses and pore water pressures is effectively captured. However, the residual effect of the pore water pressure, e.g. increase in pore pressure in a seabed, is not analysed in this study, which actually depends on the use of an elasto-plastic constitutive model of soil.
- 3) The integrated model established in this study can be used to predict the residual horizontal sliding displacements of structures under a wave impact. However, the numerical convergence problem of this new integrated model requires attention, and it needs to be solved. However, the convergence problem is a common problem when dealing with the contact problem in numerical modelling. This problem is not unique to the established integrated model.
- 4) Only a poro-elastic soil model is used in this study. However, new constitutive models of soil can be developed and integrated into ABAQUS by users through secondary development programming interfaces provided by ABAQUS. This will significantly expand the scope of engineering applications for the integrated model established in this study, in the future.

Declaration of competing interest

The authors declare that they have no known competing financial interests or personal relationships that could have appeared to influence the work reported in this paper.

Acknowledgements

We are grateful for the financial support provided by the National Natural Science Foundation of China (Project No. 51879257).

References

- [1] Franco L. Vertical breakwaters: the Italian experience. *Coast Eng* 1994;22(1–2):31–55.
- [2] Sumer BM, Fredsøe J. The mechanism of scour in the marine environment. New Jersey: World Scientific; 2002.
- [3] Chung SG, Kim SK, Kang YJ, Im JC, Prasad KN. Failure of a breakwater founded on a thick normally consolidated clay layer. *Geotechnique* 2006;3:393–409.
- [4] Madsen OS. Wave-induced pore pressures and effective stresses in a porous bed. *Geotechnique* 1978;28(4):377–93.
- [5] Yamamoto T, Koning H, Sellmeijer H, Hijum EV. On the response of a poro-elastic bed to water waves. *J Fluid Mech* 1978;87(1):193–206.
- [6] Biot MA. General theory of three-dimensional consolidation. *J Appl Phys* 1941;26(2):155–64.
- [7] Hsu JRC, Jeng D-S. Wave-induced soil response in an unsaturated anisotropic seabed of finite thickness. *Int J Numer Anal Methods GeoMech* 1994;18(11):785–807.
- [8] Jeng DS, Hsu JRC. Wave induced soil response in an early saturated seabed of finite thickness. *Geotechnique* 1996;46(3):427–40.
- [9] Tsai CP, Lee TL. Standing wave induced pore pressure in a porous seabed. *Ocean Eng* 1995;22(6):505–17.
- [10] Mase H, Sakai T, Sakamoto M. Wave-induced pore water pressures and effective stresses around breakwater. *Ocean Eng* 1994;21(4):361–79.
- [11] Ulker MB, Rahman MS, Guddati MN. Wave-induced dynamic response and instability of seabed around caisson breakwater. *Ocean Eng* 2010;37(17):1522–45.
- [12] Ulker MB, Rahman MS, Guddati MN. Breaking wave-induced response and instability of seabed around caisson breakwater. *Int J Numer Anal Methods GeoMech* 2012;36(3):362–90.

- [13] Ye JH, Jeng DS, Liu PL, Chan AH, Wang R, Zhu CQ. Breaking wave-induced response of composite breakwater and liquefaction in seabed foundation. *Coast Eng* 2014;85:72–86.
- [14] Liu PL-F, Lin P, Chang KA, Sakakiyama T. Numerical modelling of wave interaction with porous structures. *Journal of Waterway Port, Coastal and Ocean Engineering*, ASCE 1999;125(6):322–30.
- [15] Hur DS, Kim CH, Yoon JS. Numerical study on the interaction among a nonlinear wave, composite breakwater and sandy seabed. *Coast Eng* 2010;57(10):917–30.
- [16] Lara JL, Garcia N, Losada LJ. Rans modeling applied to random wave interaction with submerged permeable structures. *Coast Eng* 2006;53:395–417.
- [17] Mizutani N, Mostafa AM. Nonlinear wave-induced seabed instability around coastal structures. *Coast Eng J* 1998;40(2):131–60.
- [18] Mostafa AM, Mizutani N, Iwata K. Nonlinear wave, composite breakwater and seabed dynamic interaction. *Journal of Waterway Port, Coastal, and Ocean Engineering*, ASCE 1999;125(2):88–97.
- [19] Soghi H, Mikkola T, Hirdaris S. The influence of obliquely perforated dual-baffles on sway induced tank sloshing dynamics. *Journal of Engineering for the Maritime Environment* 2020. <https://doi.org/10.1177/1475090220961920>.
- [20] Soghi H, Mikkola T, Hirdaris S. The influence of obliquely perforated dual-baffles on sway induced tank sloshing dynamics. In: *Proceedings of the institution of mechanical engineers, Part M: journal of engineering for the maritime environment*; 2020. 1475090220961920.
- [21] Chang K, Jeng D. Numerical study for wave-induced seabed response around offshore wind turbine foundation in Donghai offshore wind farm, Shanghai, China. *Ocean Eng* 2014;85:32–43.
- [22] Lin Z, Pokrajac D, Guo Y, Jeng DS, Tang T, Rey N, et al. Investigation of nonlinear wave-induced seabed response around mono-pile foundation. *Coast Eng* 2017; 121:197–211.
- [23] Li Y, Ong MC, Tang T. Numerical analysis of wave-induced poro-elastic seabed response around a hexagonal gravity-based offshore foundation. *Coast Eng* 2018; 136:81–95.
- [24] Li Y, Ong MC, Tang T. A numerical toolbox for wave-induced seabed response analysis around marine structures in the OpenFOAM® framework. *Ocean Eng* 2020;195:106678.
- [25] Duan L, Jeng D, Wang D. PORO-FSSI-FOAM: seabed response around a mono-pile under natural loadings. *Ocean Eng* 2019:239–54.
- [26] Lin Z, Guo Y, Jeng DS, Liao C, Rey N. An integrated numerical model for wave–soil–pipeline interactions. *Coast Eng* 2016;108:25–35.
- [27] Tong D, Liao C, Jeng DS, Zhang L, Wang J, Chen L. Three-dimensional modeling of wave-structure-seabed interaction around twin-pile group. *Ocean Eng* 2017; 145:416–29.
- [28] Zhang Q, Zhou X, Wang J, Guo J. Wave-induced seabed response around an offshore pile foundation platform. *Ocean Eng* 2017:567–82.
- [29] Sui T, Zheng J, Zhang C, Jeng D, Zhang J, Guo Y, He R. Consolidation of unsaturated seabed around an inserted pile foundation and its effects on the wave-induced momentary liquefaction. *Ocean Eng* 2017;131:308–21.
- [30] Zhao HY, Jeng DS, Liao CC, Zhu JF. Three-dimensional modeling of wave-induced residual seabed response around a mono-pile foundation. *Coast Eng* 2017: 1–21.
- [31] Sui T, Zhang C, Jeng D, Guo Y, Zheng J, Zhang W, Shi J. Wave-induced seabed residual response and liquefaction around a mono-pile foundation with various embedded depth. *Ocean Eng* 2019;173:157–73.
- [32] Elsafti H. Modelling and analysis of wave-structure-foundation interaction for monolithic breakwaters. PhD thesis. Germany: Technical University of Braunschweig; 2015.
- [33] Elsafti H, Oumeraci H. A numerical hydro-geotechnical model for marine gravity structures. *Comput Geotech* 2016;79:105–29.
- [34] Ye J, Jeng DS, Wang R, Zhu CQ. A 3-D semi-coupled numerical model for fluid–structures–seabed-interaction (FSSI-CAS 3D): model and verification. *J Fluid Struct* 2013:148–62.
- [35] Ye J, Jeng DS, Wang R, Zhu CQ. Validation of a 2-D semi-coupled numerical model for fluid–structure–seabed interaction. *J Fluid Struct* 2013:333–57.
- [36] Jeng D, Ye J, Zhang J, Liu PL. An integrated model for the wave-induced seabed response around marine structures: model verifications and applications. *Coast Eng* 2013:1–19.
- [37] Ye JH, Jeng DS, Wang R, Zhu CQ. Numerical study of the stability of breakwater built on a sloped porous seabed under tsunami loading. *Appl Math Model* 2013; 37(23):9575–90.
- [38] Ye J, Jeng DS, Wang R, Zhu CQ. Numerical simulation of the wave-induced dynamic response of poro-elastoplastic seabed foundations and a composite breakwater. *Appl Math Model* 2015;39(1):322–47.
- [39] Ye J, Jeng DS, Chan AH, Wang R, Zhu QC. 3D integrated numerical model for fluid–structures–seabed interaction (FSSI): elastic dense seabed foundation. *Ocean Eng* 2016:107–22.
- [40] He K, Huang T, Ye J. Stability analysis of a composite breakwater at Yantai port, China: an application of FSSI-CAS-2D. *Ocean Eng* 2018;168:95–107.
- [41] Lu HB. The research on pore water pressure response to waves in sandy seabed. MSc thesis. Changsha, China: Changsha University of Science & Technology; 2005.
- [42] Wang YZ, Chen NN, Chi LH. Numerical simulation on joint motion process of various modes of caisson breakwater under wave excitation. *Commun Numer Methods Eng* 2006;22(6):535–45.
- [43] Cuomo G, Lupoi G, Shimosako K, Takahashi S. Dynamic response and sliding distance of composite breakwaters under breaking and non-breaking wave attack. *Coast Eng* 2011;58(10):953–69.
- [44] Kim S, Suh K. Determining the stability of vertical breakwaters against sliding based on individual sliding distances during a storm. *Coast Eng* 2014;94:90–101.